J. Plasma Phys. (2020), *vol*. 86, 825860502
Published by Cambridge University Press
doi:10.1017/S0022377820001270

Kinetic entropy-based measures of distribution function non-Maxwellianity: theory and simulations

Haoming Liang [1,2,†], **M. Hasan Barbhuiya** [2], **P. A. Cassak** [2,3], **O. Pezzi** [4,5,6], **S. Servidio** [7], **F. Valentini** [7] and **G. P. Zank** [1,8]

[1]Center for Space Plasma and Aeronomic Research, University of Alabama in Huntsville, Huntsville, AL 35899, USA

[2]Department of Physics and Astronomy, West Virginia University, Morgantown, WV 26506, USA

[3]Center for KINETIC Plasma Physics, West Virginia University, Morgantown, WV 26506, USA

[4]Gran Sasso Science Institute, Viale F. Crispi 7, I-67100 L'Aquila, Italy

[5]INFN/Laboratori Nazionali del Gran Sasso, I-67100 Assergi (AQ), Italy

[6]Istituto per la Scienza e Tecnologia dei Plasmi, CNR, Via Amendola 122/D, I-70126 Bari, Italy

[7]Dipartimento di Fisica, Università della Calabria, I-87036 Rende (CS), Italy

[8]Department of Space Science and Center for Space Plasma and Aeronomic Research, University of Alabama in Huntsville, Huntsville, AL 35899, USA

(Received 13 July 2020; revised 14 September 2020; accepted 15 September 2020)

We investigate kinetic entropy-based measures of the non-Maxwellianity of distribution functions in plasmas, i.e. entropy-based measures of the departure of a local distribution function from an associated Maxwellian distribution function with the same density, bulk flow and temperature as the local distribution. First, we consider a form previously employed by Kaufmann & Paterson (*J. Geophys. Res.*, vol. 114, 2009, A00D04), assessing its properties and deriving equivalent forms. To provide a quantitative understanding of it, we derive analytical expressions for three common non-Maxwellian plasma distribution functions. We show that there are undesirable features of this non-Maxwellianity measure including that it can diverge in various physical limits and elucidate the reason for the divergence. We then introduce a new kinetic entropy-based non-Maxwellianity measure based on the velocity-space kinetic entropy density, which has a meaningful physical interpretation and does not diverge. We use collisionless particle-in-cell simulations of two-dimensional anti-parallel magnetic reconnection to assess the kinetic entropy-based non-Maxwellianity measures. We show that regions of non-zero non-Maxwellianity are linked to kinetic processes occurring during magnetic reconnection. We also show the simulated non-Maxwellianity agrees reasonably well with predictions for distributions resembling those calculated analytically. These results can be important for applications, as non-Maxwellianity can be used to identify regions of kinetic-scale physics or increased dissipation in plasmas.

Key words: space plasma physics, plasma heating, plasma nonlinear phenomena

†Email address for correspondence: haoming.liang@uah.edu

1. Introduction

The conversion and dissipation of energy at small scales in magnetized plasmas is a crucial aspect of many phenomena of importance to heliospheric and planetary science. For example, heating of the solar corona to temperatures far greater than its surface is related to wave heating and turbulence (e.g. Heyvaerts & Priest 1983; Matthaeus *et al.* 1999*a*; Nakariakov *et al.* 1999) and magnetic reconnection underlying nanoflares (e.g. Klimchuk 2006; Zank *et al.* 2018). Local heating needs to occur in the turbulent solar wind to explain observed temperature profiles (e.g. Matthaeus *et al.* 1999*b*; Gosling 2007; Adhikari *et al.* 2017, 2020). Dynamics near and within Earth's bow shock plays an important role in setting the conditions of the plasma abutting Earth's magnetosphere (e.g. Feldman *et al.* 1982; Burgess, Möbius & Scholer 2012). Magnetic reconnection at both the dayside and the magnetotail is a crucial aspect of solar wind-magnetospheric coupling at Earth (e.g. Levy, Petschek & Siscoe 1964) and Mercury (e.g. Slavin *et al.* 2009) and dynamics in the magnetospheres of the outer planets (e.g. Vasyliunas 1983; McAndrews *et al.* 2008; Fuselier *et al.* 2020).

In collisional magnetized plasmas, the dissipation of energy at boundary layers in shocks, reconnecting current sheets and intermittent current sheets in a turbulent medium are relatively well understood. However, in many settings of interest for heliospheric and planetary sciences, the plasma is weakly collisional, so collisions are too weak to influence the boundary layers. In such settings, the boundary layers are typically set by gyroscales of the constituent plasma species. At these scales, the dynamics is dominated by kinetic physics, necessitating a kinetic description of the plasma.

Kinetic-scale dynamics historically was difficult to directly measure because it occurs on relatively short spatial and temporal scales. However, the measurement of kinetic features, including velocity distribution functions (VDFs) of the constituent plasma, is now achievable in kinetic simulations and *in situ* satellite observations. In particular, the Magnetospheric Multiscale (MMS) mission (Burch *et al.* 2016*a*) can resolve both electron and ion kinetic scales spatially and temporally, providing an unprecedented and exquisite opportunity to learn about the kinetic physics underlying reconnection (e.g. Burch *et al.* 2016*b*; Torbert *et al.* 2018), turbulence (e.g. Bandyopadhyay *et al.* 2018) and collisionless shocks (e.g. Gingell *et al.* 2017; Goodrich *et al.* 2018).

There are many theoretical and analytical approaches to studying kinetic-scale energy conversion and dissipation. In this study, we focus on one underutilized quantity: kinetic entropy, i.e. entropy defined fully within kinetic theory (e.g. Liang *et al.* (2019) and references therein). The kinetic entropy is often written as being proportional to the phase space integral of $f \ln f$, where f is the velocity distribution function of the plasma species. This is in contrast to the fluid entropy, related to p/ρ^{γ} where p is the pressure, ρ is the mass density and γ is the ratio of specific heats, which is only valid for a plasma in local thermodynamic equilibrium (for which f is a Maxwellian everywhere in space). Entropy has both desirable and undesirable properties. Its main desirable property is that it is uniquely related to irreversible dissipation in collisional systems (Boltzmann 1877), which potentially makes it a key quantity to identify regions where dissipation may be happening in systems of interest. Its main drawback is that the relation of entropy to dissipation is true for closed systems, but it is not clear that physical systems of interest can be construed as closed.

Consequently, while there have been numerous studies of the fluid form of entropy in heliospheric systems (see Liang *et al.* (2019) for references), there are only a few studies investigating kinetic entropy. Observationally, there have been attempts to measure the kinetic entropy or use entropic measures with satellite observations of, for example, Earth's magnetotail plasma sheet (Kaufmann & Paterson 2009, 2011), Earth's bow shock

(Parks *et al.* 2012), the near-Earth solar wind (Weck *et al.* 2015; Olivier, Engelbrecht & Strauss 2019) and auroral currents (Osmane, Dimmock & Pulkkinen 2019). It has also been used in a number of theoretical and numerical studies (Montgomery & Nielson 1970; Hsu, Joyce & Montgomery 1974; Krommes & Hu 1994; Leubner 2004; Watanabe & Sugama 2004; Howes *et al.* 2006; Sarazin *et al.* 2009; Schekochihin *et al.* 2009; Tatsuno *et al.* 2009; Nariyuki 2011; Nakata, Watanabe & Sugama 2012; Loureiro, Schekochihin & Zocco 2013; TenBarge & Howes 2013; Numata & Loureiro 2015; Pezzi, Valentini & Veltri 2016; Grošelj *et al.* 2017; Hesse *et al.* 2017; Pezzi 2017; Cerri, Kunz & Califano 2018; Eyink 2018; Gary *et al.* 2018; Kawazura, Barnes & Schekochihin 2019; Liang *et al.* 2019; Pezzi *et al.* 2019; Du *et al.* 2020).

We focus on the work by Kaufmann & Paterson (2009) in the present study. In their observational study of Earth's plasma sheet, they used the kinetic entropy per particle as a diagnostic in their observations. One aspect of their study was to compare the kinetic entropy per particle with its fluid counterpart. The difference between the two at a given location and time gives a measure of how 'non-Maxwellian' a plasma is, and therefore gives a measure of the importance of non-equilibrium kinetic effects. This measure of non-Maxwellianity is not unique. Other non-Maxwellianity measures include the so-called ϵ parameter (Greco *et al.* 2012) and the so-called enstrophy (Servidio *et al.* 2017).

Knowing and quantifying the non-Maxwellianity of a distribution function is potentially of great utility since dissipation is typically associated with the emergence of non-Maxwellian distribution functions and the collisional relaxation back towards Maxwellianity (e.g. Vaivads *et al.* 2016; Valentini *et al.* 2016; Matthaeus *et al.* 2020). However, we are not aware of theoretical and/or computational studies which have put the entropy-based non-Maxwellianity measure on a firm footing. In other words, what does it mean for a plasma to have a particular departure from the (equilibrium) fluid entropy?

In this study, we provide a theoretical investigation of what we call the Kaufmann and Paterson non-Maxwellianity. We show that it has equivalent forms and provide a physical interpretation of these forms. Then, we perform an analytical calculation of it for three common closed-form non-Maxwellian distribution functions, namely two beams separated in velocity space, a bi-Maxwellian, and the distribution studied by Egedal, Le & Daughton (2013) and colleagues that appears near magnetic reconnection sites. We then show that the Kaufmann and Paterson non-Maxwellianity has the undesirable property that it can diverge, and provide the underlying reason for this. We then present a new non-Maxwellianity measure that does not diverge in the same limits. The theoretical work is then tested with data from particle-in-cell (PIC) simulations of magnetic reconnection. Links between the appearance of a non-zero non-Maxwellianity and the kinetic effects taking place during the reconnection process are made. Comparisons of the analytical non-Maxwellianity expressions are made with representative distributions that naturally arise in the simulations of reconnection, revealing good agreement.

This paper is organized as follows. In § 2, we review the definition of the Kaufmann and Paterson non-Maxwellianity. In Section 3, we analyse the quantity in general, and provides analytical expressions for three common distributions. Section 4 points out issues with the existing measure, explains the cause, presents a new non-Maxwellianity measure and shows it eliminates the issues. Section 5 describes the set-up of the PIC simulations. The simulation results and comparisons to the theory are shown in § 6. Discussion and conclusions are provided in § 7. A comparison of the non-Maxwellianity measures discussed here with other quantities that have been used to identify kinetic-scale physics in weakly collisional plasmas is outside the scope of the present study, but is carried out in a companion study (Pezzi *et al.* in preparation).

2. Kaufmann and Paterson kinetic entropy-based non-Maxwellianity

Here, we review the kinetic entropy-based measure developed by Kaufmann & Paterson (2009) to measure the non-Maxwellianity of an arbitrary given distribution function $f(\boldsymbol{r}, \boldsymbol{v}, t)$ as a function of position $\boldsymbol{r}$ and velocity $\boldsymbol{v}$ at a fixed time t. (We henceforth suppress the $\boldsymbol{r}$ and t dependence for simplicity.) First, one calculates the density $n = \int \mathrm{d}^3 v f(\boldsymbol{v})$, bulk velocity $\boldsymbol{u} = (1/n) \int \mathrm{d}^3 v \boldsymbol{v} f(\boldsymbol{v})$ and effective temperature $T = (m/3nk_B) \int \mathrm{d}^3 v (\boldsymbol{v} - \boldsymbol{u})^2 f(\boldsymbol{v})$, where k_B is Boltzmann's constant and m is the mass of a particle. The Maxwellianized distribution $f_M(\boldsymbol{v})$ associated with $f(\boldsymbol{v})$ is defined as

$$f_M(\boldsymbol{v}) = n \left(\frac{m}{2\pi k_B T} \right)^{3/2} \exp(-m(\boldsymbol{v} - \boldsymbol{u})^2 / 2k_B T). \tag{2.1}$$

The local (continuous) kinetic entropy density s (e.g. (3) in Liang *et al.* 2019) of the full distribution function $f(\boldsymbol{v})$ is

$$s = -k_B \int \mathrm{d}^3 v f(\boldsymbol{v}) \ln f(\boldsymbol{v}). \tag{2.2}$$

The kinetic entropy density s_M associated with the Maxwellianized distribution $f_M(\boldsymbol{v})$ is

$$s_M = -k_B \int \mathrm{d}^3 v f_M(\boldsymbol{v}) \ln f_M(\boldsymbol{v}). \tag{2.3}$$

Equation (2.3) is analytically solvable using direct substitution of (2.1), giving

$$s_M = \frac{3}{2} k_B n \left[1 + \ln \left(\frac{2\pi k_B T}{m n^{2/3}} \right) \right]. \tag{2.4}$$

This form motivated Kaufmann & Paterson (2009) to define a non-Maxwellianity measure, which we denote $\bar{M}_{\mathrm{KP}}$, as

$$\bar{M}_{\mathrm{KP}} = \frac{s_M - s}{(3/2) k_B n}. \tag{2.5}$$

They chose to normalize to $(3/2)k_B n = c_v n$, where $c_v = (3/2)k_B$ is the specific heat per particle at constant volume for an ideal gas, so that $\bar{M}_{\mathrm{KP}}$ is dimensionless. They note, however, that the dimensions of s and s_M individually are not well defined because they include a natural logarithm of the dimensional quantity $f(\boldsymbol{v})$. This is not an issue for differences in entropy density, which can be written as having a natural logarithm of a dimensionless quantity (see also appendix B4 of Liang *et al.* (2019)).

3. Theory of the Kaufmann and Paterson non-Maxwellianity

3.1. *Basic properties of Kaufmann and Paterson non-Maxwellianity*

Here, we gather some basic properties about the Kaufmann and Paterson non-Maxwellianity measure $\bar{M}_{\mathrm{KP}}$. First, obviously, if $f(\boldsymbol{v})$ is Maxwellian, then $f_M(\boldsymbol{v}) = f(\boldsymbol{v})$ and $\bar{M}_{\mathrm{KP}} = 0$. Second, it has long been known that $f_M(\boldsymbol{v})$ is the distribution with the maximum kinetic entropy for a fixed number of particles and total energy (in the absence of electromagnetic fields, net charge and net current) (e.g. Boltzmann 1877; Bellan 2008). Thus, s_M is the maximum entropy density for a fixed number of particles and energy. Therefore, if $\bar{M}_{\mathrm{KP}} = 0$, then $f(\boldsymbol{v})$ is Maxwellian, and one expects $\bar{M}_{\mathrm{KP}}$ to be strictly non-negative. For these reasons, $\bar{M}_{\mathrm{KP}}$ is a good measure of non-Maxwellianity.

It is potentially a useful measure because it is a local measure which can identify regions with non-Maxwellian distributions. This is worthwhile to know because the rate of change of the local entropy density s is (e.g. Eyink 2018)

$$\frac{\partial s}{\partial t} + \nabla \cdot \boldsymbol{\mathcal{J}} = -k_B \int \mathrm{d}^3 v C[f(\boldsymbol{v})][1 + \ln f(\boldsymbol{v})], \tag{3.1}$$

where $\boldsymbol{\mathcal{J}} = -k_B \int \mathrm{d}^3 v \boldsymbol{v} f(\boldsymbol{v}) \ln f(\boldsymbol{v})$ is the entropy density flux and $C[f(\boldsymbol{v})]$ is the collision operator. The collision operator for a single species typically vanishes if $f(\boldsymbol{v})$ is Maxwellian, so the degree of non-Maxwellianity can be related to dissipation through collisions (e.g. Liang *et al.* accepted). Caution is necessary, however, because there are systems where dissipation occurs even if distributions are Maxwellian everywhere. One example is if the constituent species have come to equilibrium with themselves, but are at different temperatures than each other; there can be dissipation through interspecies collisions even though each distribution is Maxwellian (e.g. Grošelj *et al.* 2017; Guo, Sironi & Narayan 2017; Parashar, Matthaeus & Shay 2018; Arzamasskiy *et al.* 2019; Cerri, Grošelj & Franci 2019; Kawazura *et al.* 2019; Parashar & Gary 2019; Rowan, Sironi & Narayan 2019; Zhdankin *et al.* 2019). A second example is at an infinitely thin shock; the non-Maxwellianity is zero everywhere in such a system, but there is dissipation and entropy production at the discontinuity.

The quantity $\bar{M}_{\mathrm{KP}}$ is fluid-like, obtained from velocity space integrals of a function of the local distribution function. Thus, it should be able to be calculated using satellite, simulation, or laboratory experiment data not very different to calculating moments of the distribution function such as density or temperature.

Another important property of $\bar{M}_{\mathrm{KP}}$ is that it is independent of density, as we now derive. Dividing (2.2) by n, then adding and subtracting $[f(\boldsymbol{v})/n] \ln n$ inside the integrand and simplifying gives

$$\frac{s}{n} = -k_B \int \mathrm{d}^3 v \frac{f(\boldsymbol{v})}{n} \ln\left(\frac{f(\boldsymbol{v})}{n}\right) - k_B \ln n. \tag{3.2}$$

Using this result to directly calculate $\bar{M}_{\mathrm{KP}} = (s_M - s)/(3/2)k_B n$ reveals that the $k_B \ln n$ term cancels because the densities associated with $f(\boldsymbol{v})$ and $f_M(\boldsymbol{v})$ are the same, so

$$\bar{M}_{\mathrm{KP}} = \frac{2}{3}\left[-\int \mathrm{d}^3 v \left(\frac{f_M(\boldsymbol{v})}{n}\right) \ln\left(\frac{f_M(\boldsymbol{v})}{n}\right) + \int \mathrm{d}^3 v \left(\frac{f(\boldsymbol{v})}{n}\right) \ln\left(\frac{f(\boldsymbol{v})}{n}\right)\right]. \tag{3.3}$$

This shows that if one uses the convention where the distribution function is a probability density instead of a phase space density, i.e. $f(\boldsymbol{v}) \to f(\boldsymbol{v})/n$, then the result for $\bar{M}_{\mathrm{KP}}$ is unchanged. It also shows that $\bar{M}_{\mathrm{KP}}$ has no explicit dependence on the plasma density n.

We note that $\bar{M}_{\mathrm{KP}}$ contains similar information to the non-Maxwellianity parameter ϵ introduced by Greco *et al.* (2012) and the enstrophy non-Maxwellianity Ω (Servidio *et al.* 2017). In our notation, ϵ is

$$\epsilon = \frac{1}{n}\sqrt{\int \mathrm{d}^3 v [f(\boldsymbol{v}) - f_M(\boldsymbol{v})]^2}, \tag{3.4}$$

and $\Omega = n^2 \epsilon^2$. The latter was simplified by expanding $f(\boldsymbol{v})$ in a Hermite expansion, which relates Ω to the Hermite spectrum of $f(\boldsymbol{v})$. In the limit that the departure from

a Maxwellian is small, we can write $f(\boldsymbol{v}) = f_M(\boldsymbol{v}) + \delta f(\boldsymbol{v})$. Doing an expansion of $\bar{M}_{\rm KP}$ to second order in $\delta f(\boldsymbol{v})$ gives

$$\bar{M}_{\rm KP} \simeq \frac{1}{3n}\int \mathrm{d}^3 v \frac{[f(\boldsymbol{v}) - f_M(\boldsymbol{v})]^2}{f_M(\boldsymbol{v})}, \tag{3.5}$$

as is well known in gyrokinetic theory (e.g. Howes *et al.* 2006; Grošelj *et al.* 2017; Cerri *et al.* 2018; Kawazura *et al.* 2019). This is quadratic in $\delta f(\boldsymbol{v})$, similar to ϵ and Ω. Thus, one would expect ϵ, Ω and $\bar{M}_{\rm KP}$ to have similar structure in strongly collisional systems where the deviation from Maxwellian distributions is small. When deviations from Maxwellianity are large, the two measures likely are different. These measures are compared with each other and other dissipation measures for weakly collisional systems in a companion study (Pezzi *et al.* in preparation).

This section provides some insight into the properties of $\bar{M}_{\rm KP}$, but it does not address how to interpret what it means for the non-Maxwellianity to be a particular number. The following sections introduce three examples where analytical values of $\bar{M}_{\rm KP}$ are calculated for common non-Maxwellian distribution functions.

3.2. *Kaufmann and Paterson non-Maxwellianity for two beams*

We calculate $\bar{M}_{\rm KP}$ analytically for a two-population plasma that are each Maxwellian but drift parallel or anti-parallel to each other, and we require that the relative velocity of the beams is large enough that the overlap between the two populations in velocity space is negligible. A condition for this is derived below. The distribution function $f_{\rm beam}(\boldsymbol{v})$ for such a system is given by

$$\begin{aligned} f_{\rm beam}(\boldsymbol{v}) = {} & n_1\left(\frac{m}{2\pi k_B T_1}\right)^{3/2} \exp(-m(\boldsymbol{v} - u_{z1}\hat{\boldsymbol{z}})^2/2k_B T_1) \\ & + n_2\left(\frac{m}{2\pi k_B T_2}\right)^{3/2} \exp(-m(\boldsymbol{v} - u_{z2}\hat{\boldsymbol{z}})^2/2k_B T_2), \end{aligned} \tag{3.6}$$

where n_1 and n_2 are the densities of the two beams, u_{z1} and u_{z2} are the bulk velocities of the two beams, assumed parallel or anti-parallel, and T_1 and T_2 are the temperatures of the two individual beams. By taking moments, it is straightforward to show that the density, bulk flow and effective temperature are

$$n = n_1 + n_2, \tag{3.7}$$

$$u_z = \frac{n_1 u_{z1} + n_2 u_{z2}}{n_1 + n_2}, \tag{3.8}$$

$$T_{\rm beam} = \frac{m n_1 n_2}{3k_B(n_1 + n_2)^2}(u_{z1} - u_{z2})^2 + \frac{n_1 T_1 + n_2 T_2}{n_1 + n_2}. \tag{3.9}$$

These bulk properties are valid independent of whether the two populations overlap in velocity space. The kinetic entropy density, however, is not exactly solvable unless the overlap between the two distributions is negligible, which occurs when the first term in (3.9) dominates the second term. In that limit, the kinetic entropy density $s_{\rm beam}$ from (2.2)

is just the sum of the kinetic entropies of the individual beams,

$$s_{\rm beam} \simeq \frac{3}{2}k_B(n_1+n_2) + \frac{3}{2}k_B\left[n_1\ln\left(\frac{2\pi k_B T_1}{m n_1^{2/3}}\right) + n_2\ln\left(\frac{2\pi k_B T_2}{m n_2^{2/3}}\right)\right]. \tag{3.10}$$

Equations (2.4) and (2.5) give an associated non-Maxwellianity of

$$\bar{M}_{\rm KP,beam} \simeq \ln\left(\frac{T_{\rm beam}/n^{2/3}}{(T_1/n_1^{2/3})^{n_1/n}(T_2/n_2^{2/3})^{n_2/n}}\right). \tag{3.11}$$

As a special case, if the beams are identical plasmas ($n_1 = n_2$ and $T_1 = T_2$) and they are counter-propagating ($u_{z1} = -u_{z2}$), then

$$\bar{M}_{\rm KP,beam} \simeq \ln\left(\frac{T_{\rm beam}}{2^{2/3}T_1}\right) \simeq \ln\left(\frac{m u_{z1}^2/3 + k_B T_1}{2^{2/3}k_B T_1}\right). \tag{3.12}$$

Letting $u_{z1}^2 = \mathcal{M}^2 k_B T_1/m$ with $\mathcal{M} \gg 1$, where $\mathcal{M}$ is an effective Mach number of the flow (leaving out a factor of the ratio of specific heats γ), then the Kaufmann and Paterson non-Maxwellianity for this distribution is $\bar{M}_{\rm KP,beam} \simeq \ln[(\mathcal{M}^2/3+1)/2^{2/3}]$.

3.3. *Kaufmann and Paterson non-Maxwellianity for bi-Maxwellian distributions*

A bi-Maxwellian distribution function $f_{\rm biM}(\boldsymbol{v})$ is defined as

$$f_{\rm biM}(\boldsymbol{v}) = n\left(\frac{m}{2\pi k_B T_\perp}\right)\left(\frac{m}{2\pi k_B T_\parallel}\right)^{1/2}\exp(-m(\boldsymbol{v}-\boldsymbol{u})_\perp^2/2k_B T_\perp)\exp(-m(\boldsymbol{v}-\boldsymbol{u})_\parallel^2/2k_B T_\parallel), \tag{3.13}$$

where the $\perp$ and $\parallel$ subscripts allow for anisotropic velocities and temperatures, typically relative to the direction of a magnetic field. Straightforward calculation of the associated kinetic entropy density from (2.2) gives

$$s_{\rm biM} = \frac{3}{2}k_B n\left[1+\ln\left(\frac{2\pi k_B T_\perp^{2/3}T_\parallel^{1/3}}{m n^{2/3}}\right)\right], \tag{3.14}$$

and (2.5) gives an associated non-Maxwellianity of

$$\bar{M}_{\rm KP,biM} = \ln\left(\frac{T}{T_\perp^{2/3}T_\parallel^{1/3}}\right) = \ln\left[\frac{2}{3}\left(\frac{T_\perp}{T_\parallel}\right)^{1/3} + \frac{1}{3}\left(\frac{T_\parallel}{T_\perp}\right)^{2/3}\right], \tag{3.15}$$

where the second form eliminates the effective temperature using $T = (2/3)T_\perp + (1/3)T_\parallel$. A plot of $\bar{M}_{\rm KP,biM}$ as a function of $T_\perp/T_\parallel$ is given in black on a linear scale in figure 1. This helps give perspective on values of the Kaufmann and Paterson non-Maxwellianity measure for a bi-Maxwellian distribution function. In particular, $\bar{M}_{\rm KP,bim} = 0$ for a Maxwellian plasma ($T_\perp/T_\parallel = 1$), as expected. For example values, $\bar{M}_{\rm KP,biM} \simeq 0.17$ for $T_\perp/T_\parallel = 4$ and $\bar{M}_{\rm KP,biM} \simeq 0.23$ for $T_\perp/T_\parallel = 1/4$.

Interestingly, (3.15) reveals that $\bar{M}_{\rm KP,biM}$ diverges to infinity as $T_\perp/T_\parallel$ goes to either zero or infinity. The red line in figure 1 uses a logarithmic horizontal scale over a broader range of $T_\perp/T_\parallel$ to motivate this. The reason for the divergence is discussed in § 4.

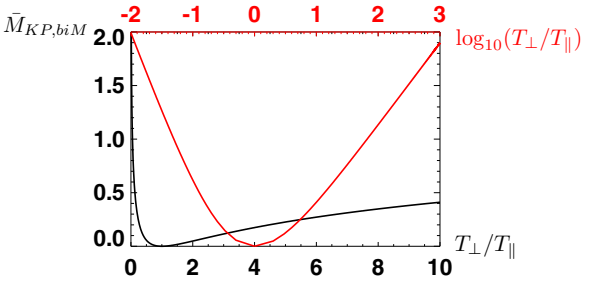

FIGURE 1. Plot of the Kaufmann and Paterson non-Maxwellianity $\bar{M}_{\mathrm{KP,biM}}$ for a bi-Maxwellian distribution function $f_{\mathrm{biM}}(\boldsymbol{v})$ as a function of the ratio of perpendicular to parallel temperature $T_\perp/T_\parallel$. The black line uses a linear horizontal scale on the bottom axis, and the red line uses a logarithmic horizontal scale on the top axis over a wider range of $T_\perp/T_\parallel$ to show that it diverges for small and large $T_\perp/T_\parallel$.

3.4. *Kaufmann and Paterson non-Maxwellianity for Egedal distributions*

During magnetic reconnection, magnetic fields in the upstream region bend as they approach the reconnection site. A magnetic field-aligned electric field accelerates electrons into this region, leading to a population of electrons that gets trapped in the mirror field (Egedal *et al.* 2013). The electron VDFs in these regions are elongated in the direction parallel to the magnetic field, leading to a gyrotropic distribution. The distribution is a double adiabatic and reversible solution to the electron drift kinetic equation obtained in the limit of short electron transit/bounce time (Egedal *et al.* 2013). Here, we call it an Egedal distribution $f_{\mathrm{Eg}}(\boldsymbol{v})$, and it is given by

$$f_{\mathrm{Eg}}(\boldsymbol{v}) = \begin{cases} n_\infty \left(\dfrac{2\pi k_B T_\infty}{m}\right)^{-3/2} \exp(-m v_\perp^2 B_\infty / 2k_B T_\infty B) & \text{trapped} \\ n_\infty \left(\dfrac{2\pi k_B T_\infty}{m}\right)^{-3/2} \exp(-m(v_\perp^2 + v_\parallel^2)/2k_B T_\infty) \exp(e\phi_\parallel / k_B T_\infty) & \text{passing} \end{cases}, \tag{3.16}$$

where n_∞, T_∞ and B_∞ are the density, temperature and magnetic field strength far upstream, B is the local magnetic field strength, $\phi_\parallel$ is the parallel acceleration potential, and $v_\perp$ and $v_\parallel$ are the speeds perpendicular and parallel to the magnetic field. The trapped/passing boundary is given by

$$\frac{1}{2} m(v_\parallel^2 + v_\perp^2) - e\phi_\parallel - \frac{1}{2}\frac{m v_\perp^2}{B} B_\infty = 0. \tag{3.17}$$

Calculating the local number density $n = \int \mathrm{d}^3 v f_{\mathrm{Eg}}(\boldsymbol{v})$ for this distribution gives (Le *et al.* 2009)

$$\frac{n}{n_\infty} = 2b\sqrt{\frac{\Phi}{\pi}} + \mathrm{erfcx}(\sqrt{\Phi}) - (1-b)^{3/2}\mathrm{erfcx}\left(\sqrt{\frac{\Phi}{1-b}}\right), \tag{3.18}$$

where $\mathrm{erfcx}(x) = \mathrm{e}^{x^2}\,\mathrm{erfc}(x) = \mathrm{e}^{x^2}[1 - \mathrm{erf}(x)]$ is the scaled complementary error function, $\mathrm{erfc}(x) = (2/\sqrt{\pi}) \int_x^\infty \mathrm{e}^{-z^2}\,\mathrm{d}z$, $b = B/B_\infty$, and $\Phi = e\phi_\parallel / k_B T_\infty$. Note, in the limit of $\Phi \to 0$ and $b \to 1$, the trapped/passing boundary from (3.17) reduces to a point at $v_\parallel = 0$, and the distribution function $f_{\mathrm{Eg}}(\boldsymbol{v})$ reduces to a Maxwellian, so the Maxwellian results should be recovered. Since $\mathrm{erfcx}(0) = 1$, we recover $n = n_\infty$ in this limit, as expected.

The kinetic entropy density s_{Eg} for an Egedal distribution follows from a direct application of (2.2). A lengthy calculation gives

$$s_{\mathrm{Eg}} = \frac{3}{2}k_B n\left[\frac{n_\infty G}{n} + \ln\left(\frac{2\pi k_B T_\infty}{m n_\infty^{2/3}}\right)\right], \tag{3.19}$$

where

$$G = 2b\sqrt{\frac{\Phi}{\pi}} + \left(1 - \frac{2\Phi}{3}\right)\mathrm{erfcx}(\sqrt{\Phi}) - \sqrt{1-b}\left(1 - b - \frac{2\Phi}{3}\right)\mathrm{erfcx}\left(\sqrt{\frac{\Phi}{1-b}}\right). \tag{3.20}$$

As a check, in the $\Phi \to 0$, $b \to 1$ limit, $G \to 1$, so (3.19) reduces to (2.4), as expected. We also note that, since $\mathrm{erfcx}(x) \to 1/(x\sqrt{\pi})$ asymptotically in the $x \to \infty$ limit, s_{Eg} diverges as $\Phi \to \infty$.

To calculate $\bar{M}_{\mathrm{KP,Eg}}$ for Egedal distributions from (2.5), one needs the effective temperature T_{Eg} for Egedal distributions to get the entropy density of the Maxwellianized distribution. The parallel temperature $T_{\parallel,\mathrm{Eg}} = [m/(nk_B)]\int \mathrm{d}^3v(v_\parallel - u_\parallel)^2 f(\boldsymbol{v})$ and perpendicular temperature $T_{\perp,\mathrm{Eg}} = [m/(2nk_B)]\int \mathrm{d}^3v(\boldsymbol{v}_\perp - \boldsymbol{u}_\perp)^2 f(\boldsymbol{v})$, following lengthy calculations, are

$$T_{\parallel,\mathrm{Eg}} = \frac{n_\infty T_\infty}{n}\left[\mathrm{erfcx}(\sqrt{\Phi}) + 2b\left(2 - b + \frac{2\Phi}{3}\right)\sqrt{\frac{\Phi}{\pi}} - (1-b)^{5/2}\,\mathrm{erfcx}\left(\sqrt{\frac{\Phi}{1-b}}\right)\right], \tag{3.21}$$

$$T_{\perp,\mathrm{Eg}} = \frac{n_\infty T_\infty}{n}\left\{\mathrm{erfcx}(\sqrt{\Phi}) + b(3b-1)\sqrt{\frac{\Phi}{\pi}} + (1-b)^{3/2}\left[\frac{\Phi b}{1-b} - \left(\frac{3b}{2} + 1\right)\right]\mathrm{erfcx}\left(\sqrt{\frac{\Phi}{1-b}}\right)\right\}, \tag{3.22}$$

$$T_{\mathrm{Eg}} = \frac{2}{3}T_{\perp,\mathrm{Eg}} + \frac{1}{3}T_{\parallel,\mathrm{Eg}}. \tag{3.23}$$

As a check, $T_{\parallel,\mathrm{Eg}}$, $T_{\perp,\mathrm{Eg}}$ and T_{Eg} all go to T_∞ in the $\Phi \to 0, b \to 1$ limit, as expected. Then, s_M is calculated from (2.4) and using the result with (3.19) and (2.5), the closed-form non-Maxwellianity $\bar{M}_{\mathrm{KP,Eg}}$ for Egedal distribution functions is

$$\bar{M}_{\mathrm{KP,Eg}} = 1 - \frac{n_\infty G}{n} + \ln\left(\frac{T_{\mathrm{Eg}}/n^{2/3}}{T_\infty/n_\infty^{2/3}}\right). \tag{3.24}$$

For reference, plots of kinetic entropy density s_{Eg} and Kaufmann and Paterson non-Maxwellianity $\bar{M}_{\mathrm{KP,Eg}}$ for an Egedal distribution are in figure 2, using a density of $n/n_\infty = 0.805$ and $T_\infty = 0.08\ B_\infty^2/4\pi k_B n_\infty$. Panels (*a*) and (*d*) are contour plots of s_{Eg} and $\bar{M}_{\mathrm{KP,Eg}}$, respectively, as a function of b and Φ. The former is normalized to $k_B n_\infty$. Panels (*b*) and (*e*) give cuts as a function of b at $\Phi = 2, 4, 6, 8$ and 10. Panels (*c*) and (*f*) give cuts as a function of Φ at $b = 0.15, 0.30, 0.45, 0.60$ and 0.75. The plots show that the non-Maxwellianity increases as Φ increases, which makes sense physically

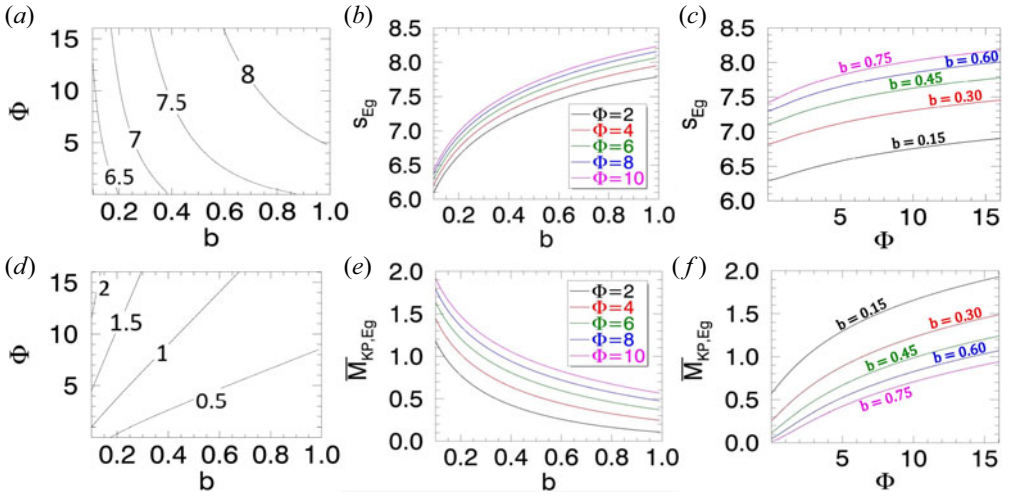

FIGURE 2. Kinetic entropy density s_{Eg} and Kaufmann and Paterson non-Maxwellianity $\bar{M}_{\mathrm{KP,Eg}}$ for an Egedal distribution function from (3.19) and (3.23) assuming $n/n_{\infty}=0.805$ and $T_{\infty}=0.08\ B_{\infty}^2/4\pi k_B n_{\infty}$. Panel (*a*) and panel (*d*) are contour plots of s_{Eg} and $\bar{M}_{\mathrm{KP,Eg}}$, respectively, as a function of $b=B/B_{\infty}$ and $\Phi=e\phi_{\parallel}/k_BT_{\infty}$. Panel (*b*) and panel (*e*) are cuts of these as a function of b for five representative values of Φ. Panel (*c*) and panel (*f*) are cuts of these as a function of Φ for five representative values of b.

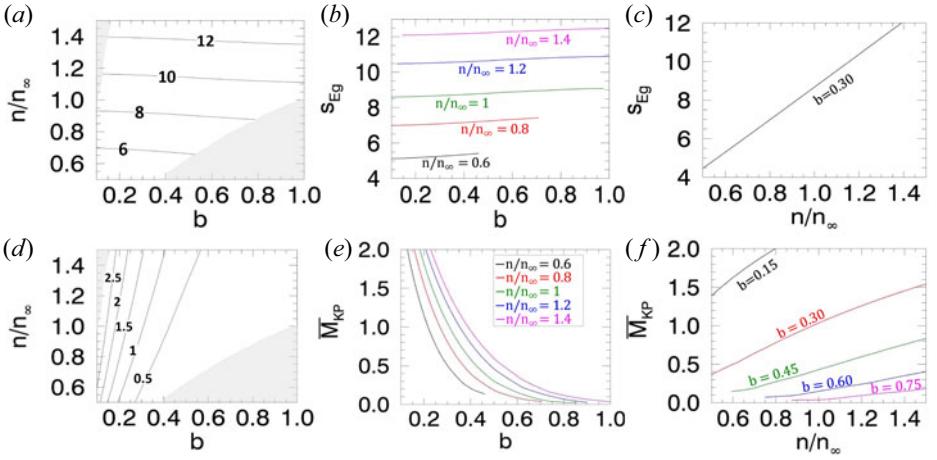

FIGURE 3. Analogous to figure 2, except plotted as a function of n/n_{∞} and $b=B/B_{\infty}$ upon inversion of (3.18). The shaded regions in panel (*a*) and panel (*d*) correspond to parameters for which the inversion gives values of Φ below 0 or above 80, and are removed from the plot.

because this increases the temperature anisotropy leading to an increase in $\bar{M}_{\mathrm{KP}}$, similar to bi-Maxwellian distributions in the previous section.

Following Le *et al.* (2009), it is typically more useful to eliminate Φ in favour of n/n_{∞} and b by numerically inverting (3.18). The result is then in terms of quantities more easily found in observations and simulations. Plots analogous to figure 2 but as a function of n/n_{∞} and b are in figure 3. Panels (*a*) and (*d*) are contour plots of s_{Eg} and $\bar{M}_{\mathrm{KP,Eg}}$, respectively. Panels (*b*) and (*e*) give cuts as a function of b for $n/n_{\infty}=0.6, 0.8, 1.0,$

1.2 and 1.4. Panels (*c*) and (*f*) give cuts as a function of n/n_∞ for fixed b; only $b = 0.3$ is shown in panel (*c*) since the dependence on b is weak, while panel (*f*) shows cuts for $b = 0.15, 0.30, 0.45, 0.60$ and 0.75. Note that numerically inverting (3.18) gives negative Φ or extremely high Φ (≥ 80) for some values of n/n_∞ and b. Such values are eliminated from the plots and are denoted by shaded grey regions in figure 3(*a*,*d*).

The past three subsections provide exact solutions for the non-Maxwellianity measure of analytic forms of three common non-Maxwellian VDFs. These are potentially useful to quantify the non-Maxwellianity of self-consistently generated distribution functions in physical systems, such as those undergoing reconnection, turbulence, or shocks in magnetized plasmas. In self-consistent plasmas, the distributions undoubtedly are not exactly given by the expressions analysed here, but should provide a reasonable approximation in some settings. A test of this will be carried out for the reconnection simulations discussed in §§ 5 and 6.4.

4. A new non-Maxwellianity measure

4.1. *Why the Kaufmann and Paterson non-Maxwellianity diverges*

Desirable properties of the Kaufmann and Paterson non-Maxwellianity measure are that it is dimensionless, non-negative and vanishes when the distribution function is Maxwellian. An undesirable property of $\bar{M}_{\mathrm{KP}}$ is that there is no upper bound, as shown in the previous section. This makes it difficult to interpret what it means for the non-Maxwellianity to have a particular value. It would be preferable to have a normalized non-Maxwellianity measure that remains finite to facilitate its interpretation.

To develop such a measure, we must elucidate the cause of the divergence of $\bar{M}_{\mathrm{KP}}$. We see that it is not an issue with the definition of the non-Maxwellianity itself, but rather a fundamental issue with the kinetic theory description. Indeed, the entropy density s_M of a Maxwellian, from (2.4), diverges for either $T \to 0$ or $T \to \infty$.

The problem arises as soon as one approximates the entropy density by the velocity space integral in (2.2) instead of the combinatorial Boltzmann entropy related to the logarithm of the number of different microstates to produce a given macrostate. The cause of the problem is the coarse graining that is necessary to formulate the kinetic theory description. As reviewed, for example, in Liang *et al.* (2019), in order to define kinetic entropy, or even a distribution function itself, one needs to break phase space into cells of hypervolume $\Delta^3 r \Delta^3 v$, where $\Delta^3 r$ is the spatial volume and $\Delta^3 v$ is the velocity space volume. The size of these cells is restricted – they cannot be too large where they do not resolve relevant structures in phase space, and they cannot be too small or the number of particles becomes too small for a statistical description. This provides insight to why the kinetic entropy diverges. As $T \to 0$, velocity space structures become strongly peaked (mathematically, they approach a δ-function), and a finite sized grid no longer resolves the structure. As $T \to \infty$ for a fixed velocity-space grid, the number of particles in each phase space cell decreases, and the statistical description of the particles breaks down.

These issues lead to unphysical results for the kinetic entropy using the standard definition from (2.2) because the kinetic entropy should not diverge in these limits. To see this, note that evaluating (2.2) for a δ-function distribution function gives an s that diverges. However, this divergence is specious. To justify this statement, we go back to the original combinatorial form of kinetic entropy given by Boltzmann in which $S = k_B \ln \Omega$, where Ω is the number of microstates corresponding to a given macrostate (see, e.g. appendix A1 of Liang *et al.* (2019)). The statistical interpretation of kinetic entropy is related to the number of ways to exchange the positions and velocities of particles in the system. For a δ-function distribution, all particles are in a single cell in velocity space,

so there is only one microstate for this macrostate. The combinatorial kinetic entropy is therefore $S = 0$. Thus, (2.2) giving $s = \infty$ is completely wrong in this limit.

Consequently, the divergence of the kinetic entropy is caused by a fundamental breakdown of kinetic theory as distributions get too broad or too peaked. The core reason for the problem is that in applications, the kinetic entropy, and indeed the distribution function itself, are only defined in a course-grained phase space, and is fundamentally an explicit function of the phase space grid scale. The formulation of kinetic entropy producing (2.2) does not capture this dependence, and this must be addressed to produce a non-Maxwellianity measure that is capable of being interpreted physically.

4.2. *The non-locality of the Kaufmann and Paterson non-Maxwellianity*

A second fundamental issue with the Kaufmann and Paterson non-Maxwellianity measure is that one desires it to be a local measure. However, the kinetic entropy density s contains information, in the combinatorial sense, about exchanging particles at different positions. Thus, using s makes the non-Maxwellianity non-local in position space. It is preferable to have the non-Maxwellianity, in the combinatorial sense, to locally describe only particles at a particular location being exchanged in velocity space. It has been shown (Mouhot & Villani 2011; Liang *et al.* 2019) that the full kinetic entropy can be decomposed into a sum of a velocity space kinetic entropy and a position space kinetic entropy. The velocity space kinetic entropy density s_{velocity} is

$$s_{\text{velocity}} = k_B \left[n \ln\left(\frac{n}{\Delta^3 v}\right) - \int \mathrm{d}^3 v f(\boldsymbol{v}) \ln f(\boldsymbol{v}) \right] = k_B n \ln\left(\frac{n}{\Delta^3 v}\right) + s. \tag{4.1}$$

We argue that this kinetic entropy is more appropriate for defining a local measure of non-Maxwellianity.

Interestingly, a non-Maxwellianity analogous to the Kaufmann and Paterson definition but using velocity space kinetic entropy density is exactly equivalent to $\bar{M}_{\text{KP}}$, i.e.

$$\bar{M}_{\text{KP}} = \frac{s_{\text{velocity},M} - s_{\text{velocity}}}{(3/2) k_B n}. \tag{4.2}$$

To see this, note that the density n of the raw distribution $f(\boldsymbol{v})$ and the density of the Maxwellian distribution $f_M(\boldsymbol{v})$ are the same by definition, so the additional term $k_B n \ln(n/\Delta^3 v)$ is the same for the raw and Maxwellianized distributions. Thus, that term drops out of $s_{\text{velocity},M} - s_{\text{velocity}}$, and the resultant non-Maxwellianity is identical to $\bar{M}_{\text{KP}}$. Thus, as far as the non-Maxwellianity measure is concerned, the Kaufmann and Paterson definition does give the desired result; the conclusion of this section is that a reinterpretation in terms of velocity space kinetic entropy density is desirable.

4.3. *A new non-Maxwellianity measure*

To address the issues discussed in the previous two sections, we propose a definition of the following normalized, non-divergent, non-Maxwellianity measure, which we denote $\bar{M}$:

$$\bar{M} = \frac{s_{\text{velocity},M} - s_{\text{velocity}}}{s_{\text{velocity},M}}. \tag{4.3}$$

This can be written equivalently as

$$\bar{M} = \frac{-\int \mathrm{d}^3 v f_M(\boldsymbol{v}) \ln f_M(\boldsymbol{v}) + \int \mathrm{d}^3 v f(\boldsymbol{v}) \ln f(\boldsymbol{v})}{n \ln\left(\frac{n}{\Delta^3 v}\right) - \int \mathrm{d}^3 v f_M(\boldsymbol{v}) \ln f_M(\boldsymbol{v})} = \frac{s_M - s}{s_M + k_B n \ln\left(\frac{n}{\Delta^3 v}\right)}. \tag{4.4}$$

It can also be written in terms of $\bar{M}_{\mathrm{KP}}$ by using (2.4) for s_M in the denominator, resulting in

$$\bar{M} = \frac{\bar{M}_{\mathrm{KP}}}{1 + \ln\left(\dfrac{2\pi k_B T}{m(\Delta^3 v)^{2/3}}\right)}. \tag{4.5}$$

The $\bar{M}$ measure retains the desirable properties of $\bar{M}_{\mathrm{KP}}$. First, it remains dimensionless; this is because a simple calculation confirms that s_{velocity} has appropriate dimensions of entropy per unit volume, unlike s for which the dimensions are not well defined (Kaufmann & Paterson 2009; Liang *et al.* 2019). Second, as with $\bar{M}_{\mathrm{KP}}$, we have $\bar{M} = 0$ if and only if the distribution function $f(\boldsymbol{v})$ is Maxwellian. Third, $\bar{M}$ is non-negative, provided that $\Delta^3 v$ is appropriately chosen. Fourth, from (4.5), $\bar{M}$ is the same whether using distribution functions as phase space densities or probability densities, as was the case for $\bar{M}_{\mathrm{KP}}$.

The $\bar{M}$ measure also addresses the issues in the previous two subsections. It is a measure of the non-Maxwellianity that is local in position space since it is based on the velocity space kinetic entropy density. Also, $\bar{M}$ retains an explicit dependence on the velocity space grid scale, which may seem undesirable but as argued in § 4.1 is actually a fundamental requirement of the formulation of entropy and distribution functions within kinetic theory. It is the presence of $\Delta^3 v$ that allows one to regularize the divergence that arises in s and s_M, which ensures $\bar{M}$ is finite for any temperature provided an appropriate velocity space grid scale is chosen to properly resolve both $f(\boldsymbol{v})$ and $f_M(\boldsymbol{v})$.

To see this, we evaluate $\bar{M}_{\mathrm{biM}}$ for a bi-Maxwellian distribution. From (4.5) and (3.15), we get

$$\bar{M}_{\mathrm{biM}} = \frac{\ln\left[\dfrac{2}{3}\left(\dfrac{T_\perp}{T_\parallel}\right)^{1/3} + \dfrac{1}{3}\left(\dfrac{T_\parallel}{T_\perp}\right)^{2/3}\right]}{1 + \ln\left(\dfrac{2\pi k_B[(2/3)T_\perp + (1/3)T_\parallel]}{m(\Delta^3 v)^{2/3}}\right)}, \tag{4.6}$$

where we use $T = (2/3)T_\perp + (1/3)T_\parallel$ in the denominator. This expression is general, for any temperatures and velocity space grid scale. To be specific, we consider a velocity space grid scale that is proportional to the thermal speed. It has been confirmed numerically that a velocity space grid scale slightly smaller than the thermal speed is a good choice for the simulations to be presented in the following two sections (Liang *et al.* 2019, accepted). However, this optimum velocity space grid scale is undoubtedly a function of numerical parameters, so it should be emphasized that the appropriate velocity space grid scale should be optimized for each application. In particular, for satellite or laboratory data, the velocity space grid scale is likely far smaller than the thermal speed in an absolute sense, though it likely still scales with the thermal speed. Letting the velocity space grid scale in the parallel and perpendicular directions be $\Delta v_\parallel = \alpha_\parallel (2k_B T_\parallel/m)^{1/2}$ and $\Delta v_\perp = \alpha_\perp (2k_B T_\perp/m)^{1/2}$, where $\alpha_\parallel$ and $\alpha_\perp$ are temperature-independent constants. With $\Delta^3 v = \alpha_\perp^2 \alpha_\parallel (2k_B T_\perp/m)(2k_B T_\parallel/m)^{1/2}$, (4.6) becomes

$$\bar{M}_{\mathrm{biM}} = \frac{\ln\left[\dfrac{2}{3}\left(\dfrac{T_\perp}{T_\parallel}\right)^{1/3} + \dfrac{1}{3}\left(\dfrac{T_\parallel}{T_\perp}\right)^{2/3}\right]}{1 + \ln\left(\dfrac{\pi}{\alpha_\perp^{4/3}\alpha_\parallel^{2/3}}\right) + \ln\left[\dfrac{2}{3}\left(\dfrac{T_\perp}{T_\parallel}\right)^{1/3} + \dfrac{1}{3}\left(\dfrac{T_\parallel}{T_\perp}\right)^{2/3}\right]}. \tag{4.7}$$

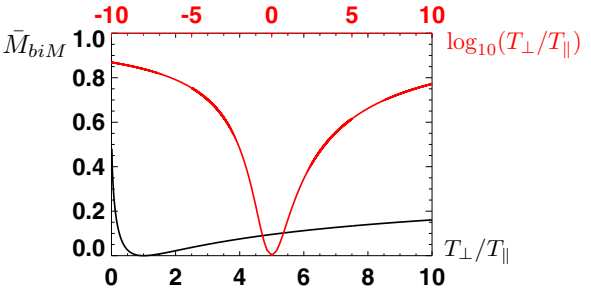

FIGURE 4. Plot of the non-Maxwellianity $\bar{M}_{\rm biM}$ for a bi-Maxwellian distribution function as a function of $T_\perp/T_\parallel$ for $\alpha_\parallel = \alpha_\perp = 1$. The black line uses a linear horizontal scale on the bottom axis. The red line uses a logarithmic horizontal scale over a wider range of $T_\perp/T_\parallel$, and motivates that $\bar{M}_{\rm biM}$ is finite even for small or large $T_\perp/T_\parallel$.

We immediately see from this form that

$$\lim_{T_\perp\to 0} \bar{M}_{\rm biM} = \lim_{T_\parallel\to 0} \bar{M}_{\rm biM} = \lim_{T_\perp\to \infty} \bar{M}_{\rm biM} = \lim_{T_\parallel\to \infty} \bar{M}_{\rm biM} = 1, \tag{4.8}$$

so the non-Maxwellianity is regularized to a maximum of 1, independent of $\alpha_\perp$ and $\alpha_\parallel$. This suggests the new non-Maxwellianity measure does have an interpretation as a fraction of the largest possible non-Maxwellianity, at least for a bi-Maxwellian distribution.A plot of $\bar{M}_{\rm biM}$ as a function of $T_\perp/T_\parallel$ is given in figure 4 for $\alpha_\perp = \alpha_\parallel = 1$. The black line is for a linear horizontal scale. Example values for this choice of the αs are $\bar{M}_{\rm biM} \simeq 0.075$ for $T_\perp/T_\parallel = 4$ and $\bar{M}_{\rm biM} \simeq 0.097$ for $T_\perp/T_\parallel = 1/4$. The red line employs a logarithmic horizontal scale using the top axis over a much broader range of $T_\perp/T_\parallel$. The plot shows that $\bar{M}_{\rm biM}$ remains finite even for small or large $T_\perp/T_\parallel$.

It is important to emphasize that the result for the non-Maxwellianity is dependent on the velocity space grid, so (4.7) and (4.8) are only valid when the velocity space grid is proportional to the thermal speed. However, it is typically not practical to have a velocity space grid that varies with temperature. Satellite instrumentation, simulation grids and laboratory diagnostics typically have a velocity space resolution that is set by other constraints and does not vary in position or time. For such cases, the general expression in (4.6) must be used for a bi-Maxwellian distribution function, or (4.5) for an arbitrary distribution function, and care must be taken to ensure $\Delta^3 v$ is chosen to properly resolve velocity space structures and preserve a good statistical description. It is also important to point out that statistics of real particles in satellite and laboratory measurements are much better than statistics of macroparticles in PIC simulations, so the allowable velocity space grid scale is undoubtedly smaller in such settings than in simulations. However, for the reasons given in earlier in this section, it is still important to reinterpret the Kaufmann and Paterson non-Maxwellianity in terms of velocity space kinetic entropy and normalize it according to (4.5).

5. Numerical simulations

5.1. *The code and simulation set-up*

In the following section, we use collisionless PIC simulations of magnetic reconnection to calculate the non-Maxwellianity measures discussed in the previous sections. Here, the numerical simulation set-up is discussed. The simulation employed here is the same simulation used in Liang *et al.* (2019), referred to there as the 'base' simulation.

Only the most relevant details are provided here and the reader is referred to that study for further details.

The code in use is P3D (Zeiler *et al.* 2002). The simulations are two-dimensional in position space and three-dimensional in velocity space. Spatial boundary conditions are periodic in both directions. Distances are normalized to the ion inertial scale d_{i0} based on a reference density n_0 that is the peak density of the initial current sheet population, magnetic fields are normalized to the upstream field strength B_0, velocities are normalized to the Alfvèn speed v_{A0} based on B_0 and n_0, times are normalized to the inverse ion cyclotron frequency Ω_{ci0}^{-1} based on B_0, temperatures are normalized to $m_i v_{A0}^2/k_B$, entropy densities are normalized to $k_B n_0$ and VDFs are normalized to $n_0 v_{A0}^3$.

The simulation domain is 51.2×25.6, and there is a double current sheet configuration with initial half-thickness of 0.5. A uniform background population has density 0.2, so the ion inertial scale d_i based on the background population is $2.24\, d_{i0}$. The initial electron and ion populations are drifting Maxwellians, with temperatures of 1/12 and 5/12, respectively, the speed of light is 15 and the ion-to-electron mass ratio is 25. The grid scale is 0.0125, the time step is 0.001 and the initial number of weighted particles per grid cell is 100; each was chosen to reduce numerical error. The velocity space grid for kinetic entropy and distribution function calculations is $1\ v_{A0} \approx 0.69 v_{\mathrm{th}0,e}$, where $v_{\mathrm{th}0,e}$ is the initial electron thermal speed; this choice was justified in Liang *et al.* (2019) and Liang *et al.* (accepted), where results for the total entropy and local entropy density were measured as a function of the velocity space grid and the results were best when the velocity space grid was slightly smaller than the species thermal speed.

5.2. *A subtlety in numerically calculating non-Maxwellianities*

There is an important numerical subtlety concerning the comparison of kinetic entropy density s based on the local distribution function $f(\boldsymbol{v})$ with the kinetic entropy density s_M based on a Maxwellianized distribution function $f_M(\boldsymbol{v})$. This is because the local distribution function consists of a finite number of macroparticles that is typically relatively small, so there is noise associated with the Monte Carlo approach of the PIC technique. We find that if one numerically calculates for n, $\boldsymbol{u}$ and T for the local distribution $f(\boldsymbol{v})$ and constructs an analytical Maxwellian $f_M(\boldsymbol{v})$ using these values, the deviation from the local kinetic entropy density is enhanced because $f(\boldsymbol{v})$ has PIC noise because it is represented by few particles and $f_M(\boldsymbol{v})$ is effectively represented by an infinite number of particles.

To avoid this undesirable disconnect, one could simply perform the simulation with a larger number of macroparticles per grid. Alternately, one can generate the Maxwellianized kinetic entropy density s_M using a separate Monte Carlo Maxwellian distribution function $f_M(\boldsymbol{v})$ using the same number of macroparticles as the local distribution function $f(\boldsymbol{v})$; we find this makes the comparison more accurate.

To do so, we create a Maxwellian entropy density look-up table. The minimum and maximum number of macroparticles, N, in the position space grid cells of interest is found. Here, N is proportional to the density, n, when the macroparticles are unweighted or the variation of the particle weights is very small in the given area. For a number of values in the range of N, Maxwellian distributions with a range of n and T are generated, and s_M is calculated for each. Then, when n and T are found at a particular position space grid cell of interest, the entropy of the Maxwellianized distribution is found by interpolating to that n and T in the look-up table for the corresponding N. The limited number of macroparticles leads to fluctuations of s_M for even the same or similar n and T. To reduce the fluctuations, we repeat the Monte Carlo generation of the Maxwellian distribution for each n and T four times, and then smooth the look-up table by averaging over the four.

There is a caution for using a look-up table when particles carry differing numerical weights. The reason is that the look-up table assumes each macroparticle carries the same weight. To address this, one can search all the spatial grids in an area of interest in the simulation box to find the variation of the particle weight in this area. If the variation is very small, then the assumption that the number of macroparticles is proportional to the density is reasonable so that the look-up table as a function of n and T is sufficient. On the other hand, in regions with large variation of particle weight, errors are introduced due to the look-up table. A three-dimensional look-up table as a function of n, T and the number of macroparticles N would be needed; this is not carried out for the present study.

6. Results

6.1. *Validation of the numerical implementation*

Here, we validate the numerical implementation of the Kaufmann and Paterson non-Maxwellianity measure $\bar{M}_{\mathrm{KP}}$ discussed in § 2. The most basic metric for validation is whether the kinetic entropy density s and non-Maxwellianity $\bar{M}_{\mathrm{KP}}$ give the expected values when the distribution function is Maxwellian. In the simulation described in § 5, the distributions far upstream from the reconnecting region are essentially Maxwellian throughout the simulation, so we first check to see the numerically generated values are as expected.

To do so, the local kinetic entropy density s is calculated at every spatial cell using the techniques discussed in Liang *et al.* (2019). The associated entropy density s_M of the Maxwellianized distribution function is calculated using a look-up table as described in § 5.2. From these, the non-Maxwellianity $\bar{M}_{\mathrm{KP}}$ is calculated using (2.5). The Kaufmann and Paterson non-Maxwellianity $\bar{M}_{\mathrm{KP}}$ at time $t = 41$ is given in figure 5, zoomed in to a portion of the computational domain near the X-point and in the outflow region for (*a*) electrons and (*b*) ions, respectively. The coordinate system is relative to the location of the X-point (x_0, y_0), so that the X-point is at the origin in these plots. A vertical cut through the X-point is shown in panel (*c*) for electrons (red) and ions (blue). For both electrons and ions, the non-Maxwellianity is near zero in the upstream regions (beyond 1 $d_i \simeq 2.24\, d_{i0}$ upstream of the reconnection site), as desired. When we use an entropy density of the Maxwellianized distribution function based on the analytical value for the fluid density, bulk flow and effective temperature from the simulation instead of the look-up table, the kinetic entropy density s_M within the current sheet is slightly lower than the kinetic entropy density from the look-up table by ∼0.01 to 0.04 (∼5 %) for the simulation performed here.

Looking holistically at the rest of the domain, the value of $\bar{M}_{\mathrm{KP}}$ is mostly non-negative for both species, as expected from § 3.1. Numerical effects due to the finite number of macroparticles in the simulation lead to fluctuations and potentially small negative values for $\bar{M}_{\mathrm{KP}}$. This suggests the implementation of the kinetic entropy in the simulations and the look-up table is valid, and underscores the importance of using the look-up table for the entropy of the Maxwellianized distribution function for the number of macroparticles per grid in use in the present simulations.

6.2. *Interpreting the non-Maxwellianity*

We now revisit figure 5 to investigate the non-Maxwellianity of the plasma in the regions affected by reconnection, with a goal of relating the non-Maxwellianity to known physical processes in reconnection. Panels (*a*) and (*b*) show that both electrons and ions depart significantly from zero non-Maxwellianity in the diffusion region $-5 < x - x_0 < 5$ and $-2 < y - y_0 < 2$. Both also depart significantly from zero in the reconnection exhaust $5 < x - x_0 < 8$. There is a magnetic island roughly at $x - x_0 > 8$.

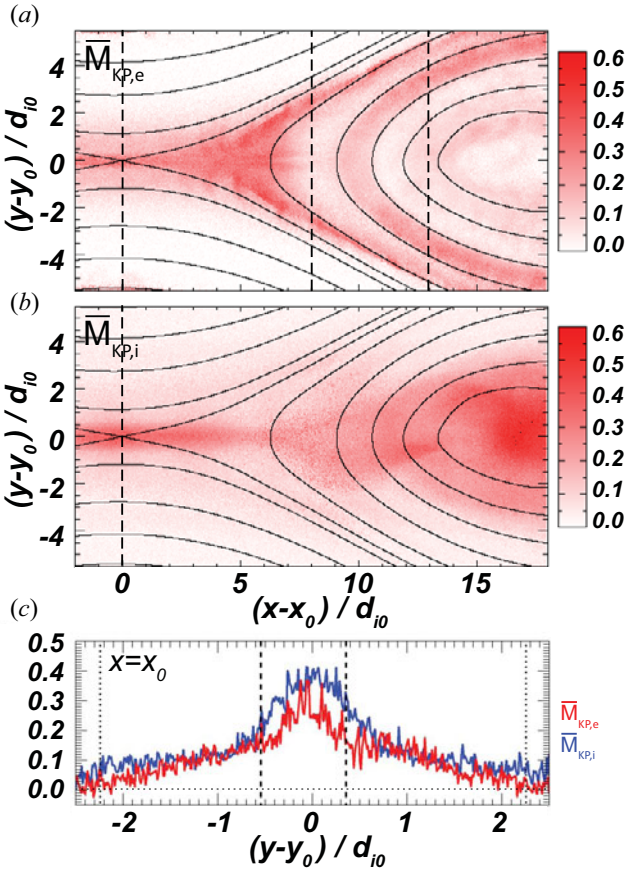

FIGURE 5. Two-dimensional plots of the Kaufmann and Paterson non-Maxwellianity at $t = 41$, where the location of the X-point at this time is (x_0, y_0), for (a) electron $\bar{M}_{\mathrm{KP},e}$ and (b) ions $\bar{M}_{KP,i}$. Black solid lines are magnetic field lines. Vertical dashed lines in panel (a) at $x - x_0 =$ 0, 8 and 13 indicate cuts that are investigated further in figures 7–9. (c) Vertical cuts of $\bar{M}_{\mathrm{KP},e}$ (red) and $\bar{M}_{KP,i}$ (blue) through the X-point in the y direction. The vertical dashed and dotted lines mark the edges of the non-frozen-in region for electrons and ions, respectively.

Panel (a) reveals that $\bar{M}_{\mathrm{KP},e}$ for the electrons has its largest departures from zero in the diffusion region, along the separatrices, and at the boundary of the island. In contrast, panel (b) shows that $\bar{M}_{KP,i}$ departs from zero in the diffusion region and in the core of the island. These regions are consistent with where we expect electrons and ions to be non-Maxwellian. Electrons accelerate due to the reconnection electric field and undergo non-adiabatic motion in the electron diffusion region, form counter-streaming beams and electron holes near separatrices, and are Fermi-accelerated and heated in the magnetic island (Drake *et al.* 2006). For ions, they undergo acceleration and non-adiabatic motion in the ion diffusion region, form counter-streaming beams and pickup ion acceleration in the exhaust (Drake *et al.* 2009), and are reflected by the moving jet front in the magnetic islands. The physical picture will be confirmed for electrons by investigating distribution functions in § 6.4.

The vertical cuts of non-Maxwellianity through the X-point shown in figure 5(c) more clearly shows that the departure from zero occurs for both species near 1 $d_i \simeq 2.24\ d_{i0}$

upstream from the X-point. By inspecting traces of the ion inflow velocity v_{iy} and $(\boldsymbol{E}\times\boldsymbol{B})_y/B^2$ (not shown), we find the ion bulk inflow deviates from the $\boldsymbol{E}\times\boldsymbol{B}$ drift speed at approximately $|y-y_0|\simeq 2.25\simeq 1\ d_i$. This deviation defines the upstream edge of the ion diffusion region and is denoted by the two vertical dotted lines in panel (c). Therefore, the ion non-Maxwellianity $\bar{M}_{KP,i}$ begins to depart from zero at the edge of the ion diffusion region, which is where ions are expected to become demagnetized and therefore their distributions become non-Maxwellian. Interestingly, $\bar{M}_{\mathrm{KP},e}$ also departs from 0 starting at the edge of the ion diffusion region, i.e. outside the electron diffusion region defined by where v_{ey} differs from $(\boldsymbol{E}\times\boldsymbol{B})_y/B^2$. As we will show in § 6.4, this corresponds to the region of electron trapping upstream of the electron diffusion region discussed extensively by Egedal and colleagues (Egedal *et al.* 2013). Both ion and electron non-Maxwellianity measures increase in magnitude as one approaches the X-point.

The upstream edges of the electron diffusion region are denoted by the vertical dashed lines at $y-y_0\simeq 0.35$ and -0.55 in panel (c); the electron diffusion region therefore has a half-width of $0.45\ d_{i0}=2.25\ d_{e0}\simeq 1\ d_e$, where d_{e0} and d_e are the electron inertial lengths based on the density n_0 and the background plasma density 0.2, respectively. Both electrons and ions see larger increases to their non-Maxwellianity in the electron diffusion region. This suggests that the non-Maxwellianity could be potentially useful as one approach among many to identify reconnection diffusion regions.

6.3. *The new non-Maxwellianity measure*

Here, we plot the new non-Maxwellianity measure discussed in § 4.3. Data analogous to figure 5 for $\bar{M}_{\mathrm{KP}}$ are plotted in figure 6 for $\bar{M}$. The spatial structure of the two measures are quite similar. This is to be expected from (4.5), since $\bar{M}$ is proportional to $\bar{M}_{\mathrm{KP}}$ and the argument in the denominator is inside a natural logarithm so there is only a weak dependence on temperature. The range of values for $\bar{M}$ is from 0 to ∼0.10 for electrons and 0 to 0.15 for ions.

6.4. *Analysis of electron distributions and non-Maxwellianity*

Here, we investigate the non-Maxwellianity parameters in relation to distribution functions measured in the simulations. This allows us to ensure the non-Maxwellianity measures are correctly identifying distributions that are non-Maxwellian, to associate physical features with the non-Maxwellianity, and to quantify non-Maxwellianity measures in the context of the exact solutions in §§ 3.2–3.4 and 4.3. We treat distributions at the three cuts denoted by the vertical dashed lines in figures 5(a) and 6(a), which are at $x-x_0=0$, 8 and 13. For brevity, we only treat electrons. Results are shown in figures 7–9, respectively. In each figure, panel (a) shows the Kaufmann and Paterson electron non-Maxwellianity $\bar{M}_{\mathrm{KP},e}$ in black and the electron non-Maxwellianity $\bar{M}_e$ in red as a function of $y-y_0$. Each has six $y-y_0$ positions marked by blue vertical dashed lines. In panel (b) of each figure, the reduced VDFs, i.e. the VDF with the third dimension integrated out, at the six marked positions are plotted. For $x-x_0=0$ (figure 7), the VDFs are plotted in the (v_{ex}, v_{ey}) plane. For $x-x_0=8$ and 13 (figures 8 and 9), the VDFs are plotted in the $(v_\parallel, v_{\perp 1})$ plane, where $v_\parallel$ is in the local direction of the magnetic field and $v_{\perp 1}$ is in the local $\boldsymbol{E}\times\boldsymbol{B}$ direction.

We begin with the plots at $x-x_0=0$ in figure 7. At this x location, except at $y-y_0=0$, the x direction is approximately parallel to the local magnetic field and y is perpendicular to it in the simulation plane. At $y-y_0=-4.7, -3.7, -2.7$, the non-Maxwellianities $\bar{M}_{\mathrm{KP},e}$ and $\bar{M}_e$ are close to zero and the VDFs resemble isotropic Maxwellian distribution functions, as is expected to be the case outside the ion diffusion region.

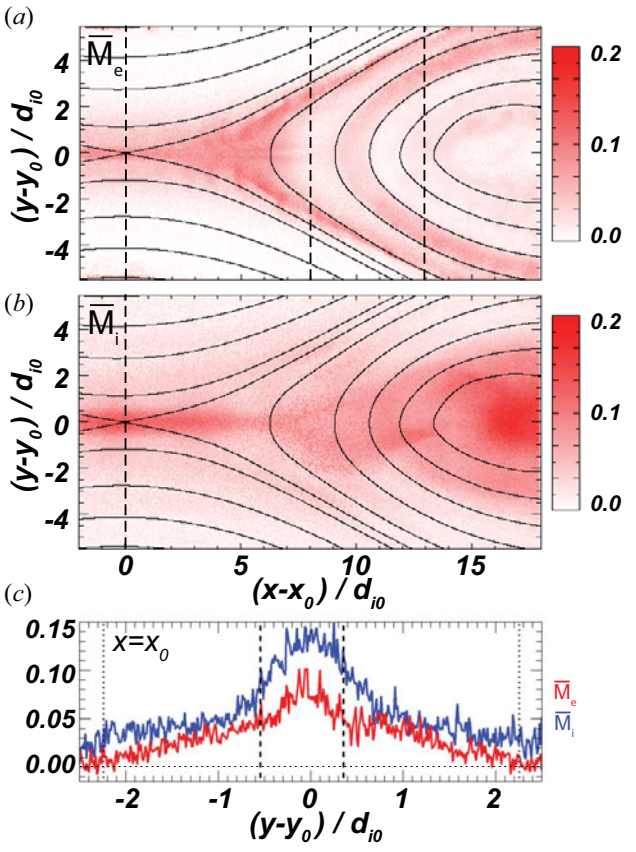

FIGURE 6. Same as figure 5 but for the non-Maxwellianity measure $\bar{M}$.

At $y - y_0 = -1.7$ and -0.7, inside the ion diffusion region, $\bar{M}_{\mathrm{KP},e}$ and $\bar{M}_e$ are non-zero. At these locations, the distributions are elongated in the direction parallel to the magnetic field. This is due to trapped electrons just upstream of the electron diffusion region (Egedal *et al.* 2013), as discussed in § 3.4. A quantitative comparison with predictions from that section would be desirable, but it requires having asymptotic values in a region with Maxwellian distributions. This is not achieved in the small simulation carried out here. However, we estimate the value as best we can for this simulation. For the $y - y_0 = -0.7$ case, we start by integrating the parallel electric field along the magnetic field from x_0 to the point where $E_\parallel$ becomes negative. We have to stop the integration at this point because the simulation domain is not large enough to reach a plasma that is Maxwellian as one goes out along the magnetic field line. Proceeding anyway, we estimate the relevant necessary input parameters from the simulation at $(x - x_0, y - y_0) = (0, -0.7)$, which are collected in the first row in table 1. Using (3.18)–(3.20), we get $s_{\mathrm{Eg}} \approx 1.04$, and using (3.21)–(3.22), we get $T_{\mathrm{Eg}} = 0.078$. Then, the predicted non-Maxwellianities $\bar{M}^{\mathrm{pred}}_{\mathrm{KP},e}$ and $\bar{M}^{\mathrm{pred}}_{e}$ are calculated from (3.23) and (4.5), and are provided in table 1. Despite the simulation size being too small, the prediction agrees within 20 % of the simulated values $\bar{M}^{\mathrm{sim}}_{\mathrm{KP},e}$ and $\bar{M}^{\mathrm{sim}}_{e}$ at $y - y_0 = -0.7$ in the simulation as seen in figure 7(*a*) and given numerically in the table. As one goes further away in y from the X-point, the agreement gets worse, which is a result of our system size not being large enough. At $y - y_0 = 0$,

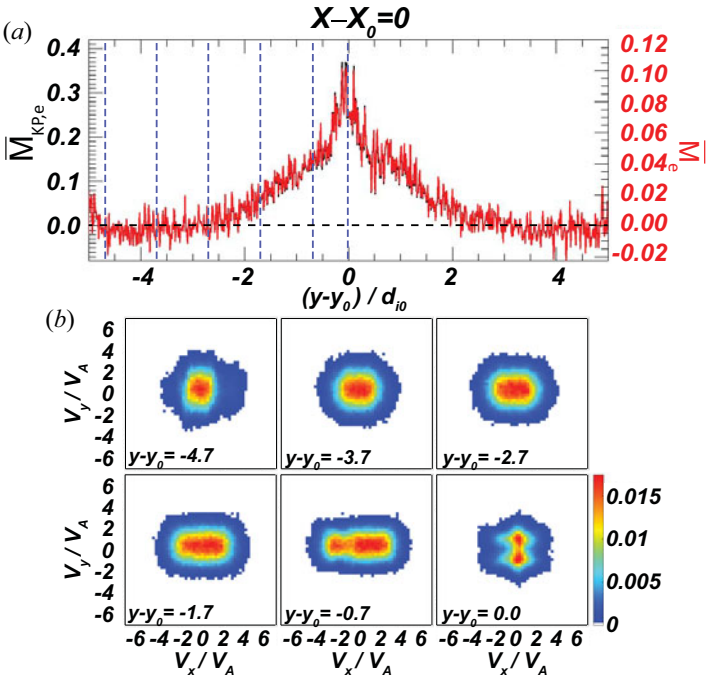

FIGURE 7. (*a*) Non-Maxwellianity measures $\bar{M}_{\mathrm{KP},e}$ (black) and $\bar{M}_e$ (red) in a vertical slice through $x - x_0 = 0$ at $t = 41$. (*b*) Reduced electron VDFs in the (v_x, v_y) plane at $x - x_0 = 0$ and $y - y_0 = -4.7, -3.7, -2.7, -1.7, -0.7$ and 0.0, denoted by the vertical dashed lines in panel (*a*).

the electrons form a beam in the out-of-plane z direction (not shown) due to being accelerated by the reconnection electric field as they undergo meandering motion (e.g. Ng *et al.* 2011). The VDF is significantly different than an isotropic Maxwellian. Indeed, this point is the local maximum of the non-Maxwellianity $\bar{M}_{\mathrm{KP},e}$ and $\bar{M}_e$ in panel (*a*).

We turn to $x - x_0 = 8$, shown in figure 8. At this x location, the separatrices are at $y - y_0 \simeq \pm 3$, so $|y - y_0| < 3$ is the exhaust and $|y - y_0| > 3$ is in the upstream region. The VDFs at $y - y_0 = \pm 3.25$ show inflowing cold electron beams anti-parallel ($y - y_0 = -3.25$) and parallel ($y - y_0 = 3.25$) to the magnetic field as they convect in towards the X-point. The VDFs at $y - y_0 = \pm 1.25$ show the hotter electron beams in the exhaust flowing in the opposite direction inside the separatrix. These flows are the well known Hall currents that result in the Hall magnetic field (Sonnerup 1979). The non-Maxwellianity in these locations is non-zero, but is relatively low because the VDF does not differ much from a Maxwellian.

At $y - y_0 = \pm 2.25$, between these two locations, there are counter-streaming signatures due to populations from both beams. While the two beams are not totally separated in velocity space, we check to see if the non-Maxwellianity is reasonably well reproduced by the analytical prediction for two beams from § 3.2. For the distribution at $(x - x_0, y - y_0) = (8, 2.25)$, we take a cut along $v_{\perp 1} = 0$ and fit the two populations with Maxwellians. The resulting plasma parameters are given in the second row of table 1. From (3.9), $T_{\mathrm{beam}} = 0.0974$, and (3.11) gives $\bar{M}^{\mathrm{pred}}_{\mathrm{KP},e}$ given in the table, along with the associated $\bar{M}^{\mathrm{pred}}_{e}$ from (4.5). The measured values $\bar{M}^{\mathrm{sim}}_{\mathrm{KP},e}$ and $\bar{M}^{\mathrm{sim}}_{e}$ are given in the table; they are within 22 %

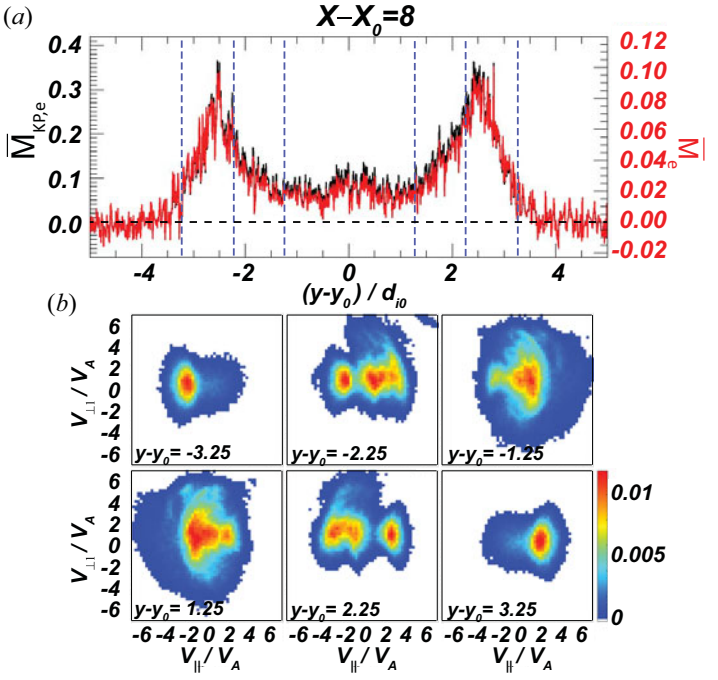

FIGURE 8. Similar to figure 7 except at $x - x_0 = 8$. The vertical dashed lines in panel (a), where the VDFs are plotted in panel (b), are at $y - y_0 = \pm 3.25$, ± 2.25 and ± 1.25. Here, the reduced distribution functions are plotted in the $(v_\parallel, v_{\perp 1})$ plane.

of the predicted values for non-overlapping counter-streaming beams, which is reasonably close.

Finally, we look further downstream cutting mostly through the interior of a magnetic island at $x - x_0 = 13$ in figure 9. At $y - y_0 = -4.7$ and -4.2, the VDFs display signatures of counter-propagating beams along the magnetic field, similar to $y - y_0 = -2.25$ in figure 8. The non-Maxwellianity is elevated there. At $y - y_0 = -3.7$, the VDF is in a region near the separatrix of a secondary X-point in the outflow that had formed before $t = 41$. Multiple electron beams are visible, due to the bouncing of electrons in the island. They lead to a relatively large value of $\bar{M}_{\mathrm{KP},e}$ and $\bar{M}_e$. Closer to the neutral line, as $y - y_0$ goes from -2.7 to -1.7 to -0.7, the multiple beams have thermalized and form hot electron distributions that are elongated along the parallel direction. This is a signature of Fermi acceleration in a contracting island (Drake *et al.* 2006). Assuming the VDF is similar in both perpendicular directions, we check to see if the analytical prediction of $\bar{M}_{\mathrm{KP}}$ for a bi-Maxwellian distribution is in reasonable agreement with the simulation result. For the distribution at $(x - x_0, y - y_0) = (13, -0.7)$, we fit Maxwellians to the $v_\parallel = 0$ and $v_{\perp 1} = 0$ cuts of this VDF; the resulting $T_\perp$ and $T_\parallel$ are in the third row of table 1. Using (3.15) and (4.6), the predicted non-Maxwellianities $\bar{M}^{\mathrm{pred}}_{\mathrm{KP},e}$ and $\bar{M}^{\mathrm{pred}}_{e}$ are shown in the table. The simulated values $\bar{M}^{\mathrm{sim}}_{\mathrm{KP},e}$ and $\bar{M}^{\mathrm{sim}}_{e}$ are shown in the table, as well, showing agreement with the predicted values within 10–20 %.

In summary, the non-Maxwellianity measures $\bar{M}_{\mathrm{KP},e}$ and $\bar{M}_e$ can be reliably implemented as diagnostics in kinetic PIC simulations. These local measures can be plotted as function of space and time, and are capable of easily identifying where

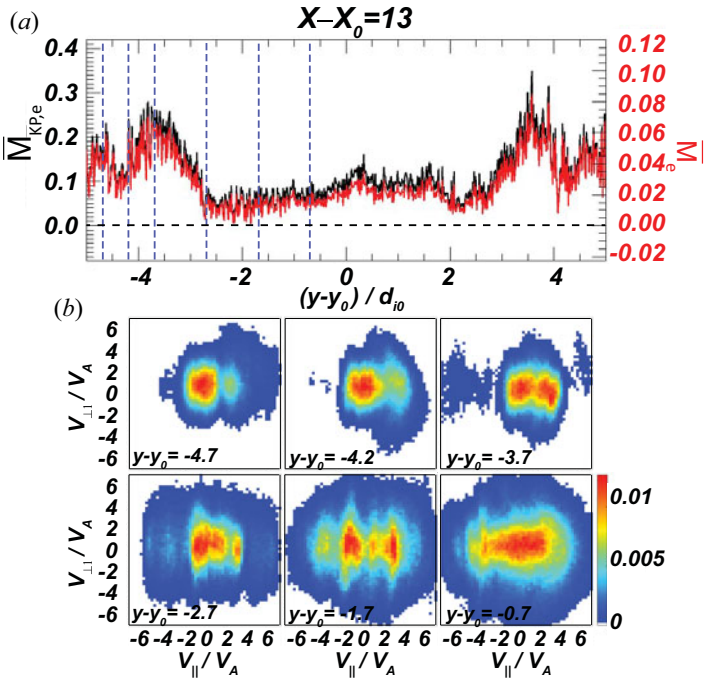

FIGURE 9. Similar to figure 8 except at $x - x_0 = 13$. The locations of the distributions are at $y - y_0 = -4.7, -4.2, -3.7, -3.2, -2.7, -1.7$ and -0.7.

distribution functions are non-Maxwellian, both for electrons and ions. For magnetic reconnection, the locations of elevated non-Maxwellianity coincide with kinetic-scale physical processes related to particle acceleration and non-adiabatic particle motion. The VDFs in regions of non-zero simulated non-Maxwellianity are, indeed, non-Maxwellian, and the analytic calculations in § 3 are capable of motivating the relative size of the non-Maxwellianity in some regions within ∼20 % despite a variation of the non-Maxwellianities by over a factor of four.

7. Discussion and conclusions

We investigate a number of aspects of kinetic entropy-based measures of the non-Maxwellianity of a given distribution function $f(\boldsymbol{v})$. The first, which we call $\bar{M}_{\mathrm{KP}}$ and is given in (2.5), was developed by Kaufmann & Paterson (2009) and used to analyse observational data of Earth's plasma sheet. Their measure is the difference between the local kinetic entropy density $s = -k_B \int \mathrm{d}^3 v f(\boldsymbol{v}) \ln f(\boldsymbol{v})$ and the kinetic entropy density s_M of the Maxwellianized distribution function $f_M(\boldsymbol{v})$ based on the low-order fluid moments of the full distribution function $f(\boldsymbol{v})$, and normalized to the number density and the specific heat per unit volume for an ideal gas. As stated by Kaufmann and Paterson, this non-Maxwellianity is a good measure because it is non-negative and only vanishes when $f(\boldsymbol{v})$ is Maxwellian. Moreover, when collisions are present, regions of non-Maxwellianity are regions in which collisions are expected to be important, so the locations of elevated non-Maxwellianity are also those in which irreversible dissipation is more prone to occur (e.g. Pezzi *et al.* 2016; Pezzi *et al.* 2019).

We are unaware of previous work to develop a quantitative understanding of $\bar{M}_{\mathrm{KP}}$, so in this study we derive closed-form analytical expressions for the non-Maxwellianity

Name	$(x-x_0, y-y_0)$	Input from simulations	$\bar{M}_{\mathrm{KP},e}^{\mathrm{pred}}$	$\bar{M}_e^{\mathrm{pred}}$	$\bar{M}_{\mathrm{KP},e}^{\mathrm{sim}}$	$\bar{M}_e^{\mathrm{sim}}$
Egedal	(0,-0.7)	$n=0.15, n_\infty=0.186, \phi_\parallel=0.070,$ $T_\infty=0.08, B_\infty=0.51, B=0.29,$ $\Rightarrow n/n_\infty=0.805, b=0.57, \Phi=0.88$	0.151	0.0430	0.13	0.037
Beam	(8, 2.25)	$n_1=0.0457, u_{z1}=2.455, T_1=0.0350,$ $n_2=0.114, u_{z2}=-1.80, T_2=0.0534$	0.323	0.0868	0.26	0.068
Bi-M	(13, −0.7)	$T_\perp=0.197, T_\parallel=0.425$	0.0700	0.0147	0.079	0.017

TABLE 1. Comparison of analytic non-Maxwellianities to simulation results. The first column gives the name of the distribution, and the second gives the location of the simulated distribution (figures 7–9) for $x-x_0=0$, 8 and 13, respectively. The third column gives the necessary plasma parameters for the given analytic distribution extracted from the simulations, given in normalized code units. The fourth and fifth columns give the predicted $\bar{M}_{\mathrm{KP},e}^{\mathrm{pred}}$ and $\bar{M}_e^{\mathrm{pred}}$ for each model, and the sixth and seventh columns give the measured values $\bar{M}_{\mathrm{KP},e}^{\mathrm{sim}}$ and $\bar{M}_e^{\mathrm{sim}}$ from the simulations.

for common non-Maxwellian distributions, including two parallel or anti-parallel beams well-separated in velocity space (§ 3.2), bi-Maxwellian distribution functions for anisotropic plasmas (§ 3.3) and Egedal distributions that arise near magnetic reconnection sites (§ 3.4).

In addition, we show that there are undesirable features of $\bar{M}_{\mathrm{KP}}$. The measure can diverge in various physical limits (especially related to temperature going to zero or infinity). This makes it difficult to interpret what a particular numerical value for $\bar{M}_{\mathrm{KP}}$ means. We argue that the reason for this is that the measure is based on the kinetic entropy density, which beyond being the kinetic entropy per unit volume does not have a physical interpretation of entropy, and it does not even have the units of entropy density. Rather, the velocity space entropy density (Mouhot & Villani 2011; Liang *et al.* 2019) has appropriate units and a physical interpretation of the number of ways to exchange the velocities of particles in the distribution in velocity space at a given position and time, thus being a more physically meaningful measure of the local kinetic entropy density associated with a given distribution function $f(\boldsymbol{v})$.

We introduce a new non-Maxwellianity measure $\bar{M}$ based on the velocity space kinetic entropy density. We show it is proportional to $\bar{M}_{\mathrm{KP}}$ (see (4.5)), with a denominator that regularizes the measure because it has explicit dependence on the velocity space grid scale. This dependence is not a hindrance, but rather is a feature, as it captures the physical effect that the kinetic entropy does depend on the velocity space grid scale.

We then use collisionless PIC simulations of two-dimensional anti-parallel magnetic reconnection, the same simulation studied in detail in Liang *et al.* (2019), to study the non-Maxwellianity measures numerically. We validate the numerical implementation of the non-Maxwellianity measure. When the number of particles per grid cell is not exceedingly high, we find that it is important to use a look-up table for the entropy density of the Maxwellianized distribution function so that it has the same level of numerical error as the raw distributions. We show that, for the simulation considered here, the non-Maxwellianity measure is non-zero where kinetic-scale processes drive VDFs away from Maxwellianity. We also show the analytic calculations in § 3 give reasonable agreement with appropriate naturally occurring distributions, within ∼20 % of the numerically calculated non-Maxwellianity.

We argue that the non-Maxwellianity, in concert with other measures, can be useful to help interpret satellite observations, laboratory experiments and kinetic numerical simulations. We suggest that $\bar{M}_{\mathrm{KP},e}$ and $\bar{M}_e$ could be useful to identify and evaluate the dynamics of plasma dissipation, such as regions of interest like electron and ion diffusion regions in reconnection, intermittent current sheets in turbulence and boundary layer physics in collisionless shocks (provided the resolution of the measurements is high enough to resolve kinetic-scale structures). These local measures can be plotted as functions of space and time, and are capable of identifying spatial regions where distribution functions are non-Maxwellian, both for electrons and ions. Now that satellites routinely measure plasma distribution functions at very high resolution, measuring non-Maxwellianity in real data is achievable, as was shown in previous studies of the enstrophy non-Maxwellianity using MMS mission data (Servidio *et al.* 2017). This will be undertaken for entropy-based non-Maxwellianity measures in future work. To get a feel for the required sensitivity, the simulation here suggests that $\bar{M}_{\mathrm{KP},e}$ is up to $\sim$0.6, corresponding to a difference of kinetic entropy per particle $(s_M - s)/n$ of $1.2 \times 10^{-23}\,\mathrm{J\,K^{-1}} = 7.8 \times 10^{-5}\,\mathrm{eV\,K^{-1}}$.

It is worth discussing the results of the present study in light of the observational results in Kaufmann & Paterson (2009). In their observational study, Geotail data from 10 years of ion measurements in one minute bins was used and averaged, and binned over spatial regions of Earth's plasma sheet. Their results reveal non-Maxwellianities (their figure 5) of the order of 1.4–2 throughout the entire plasma sheet. These values greatly exceed the values for $\bar{M}_{KP,i}$ observed in our reconnection simulations (our figure 5). There are numerous reasons for the significant difference. One is that the parameters of our simulation and the parameters in the 10 year study may not be commensurate. Another potential issue is that their fluid entropy was calculated from the fluid variables using the analytic expression, and this could cause an offset in the manner discussed in § 5.2, which would inflate the measured non-Maxwellianity. In addition, the Geotail data came from one minute averages, which undoubtedly captured variations in plasma parameters such as density and temperature, which would introduce non-Maxwellianities that may not be present from a higher time resolution measurement. Satellite data also often does not capture the cold plasma population, which requires assumptions for calculating entropy and may introduce uncertainties. Using, for example, MMS data, will be a more direct comparison with the simulation results presented here, and will be pursued in future work.

While the non-Maxwellianity is a potentially useful measure to aid the interpretation of data and simulations, a number of aspects should be kept in mind. First, a non-zero non-Maxwellianity can indicate reversible and irreversible processes, i.e. it is not necessarily purely irreversible. Moreover, it is true that non-Maxwellianity identifies regions where irreversible dissipation is prone to occur through collisions, but if collisions are entirely absent then the non-Maxwellianity is not associated with irreversible dissipation. To address this more fully requires comparisons with collisional simulations, which will be addressed in the companion study (Pezzi *et al.* in preparation). Also, since the non-Maxwellianity is local in position space, it is not capable of identifying if a plasma element has undergone an entropy change as it evolves, i.e. in a Lagrangian reference frame.

An ambiguity of the non-Maxwellianity is that there is not a one-to-one correspondence between a particular value of it and an associated distribution function or physical process. Rather, to understand it quantitatively, one still needs information about the structure of the distribution function, such as whether it consists of beams or bi-Maxwellian plasmas. However, once that link is established, the value of $\bar{M}$ can give perspective about the plasma, including allowing the inference of quantities such as the temperature anisotropy.

In addition, it provides information about what fraction of the kinetic entropy density a given distribution function has given up relative to its associated Maxwellian value, which has the maximum kinetic entropy for a fixed number of particles and total energy. Further work on interpreting such results would be worthwhile. On the other hand, there are independent efforts underway to identify structures in complicated distribution functions by breaking them into separate populations (e.g. Goldman *et al.* 2020), which could be used to aid in the interpretation of the entropy-based results.

The kinetic entropy density and non-Maxwellianity should be used in concert with other diagnostics and measures of plasma processes to contribute to its interpretation. A number of other measures have been developed; the non-Maxwellianity and these other measures will be compared and contrasted in simulations of magnetic reconnection and plasma turbulence in collisionless and collisional kinetic simulations in a companion study (Pezzi *et al.* in preparation).

Acknowledgements

This manuscript was prepared for a special issue associated with Vlasovia 2019: The Sixth International Workshop on the Theory and Applications of the Vlasov Equation. We acknowledge many helpful conversations at the workshop. We also acknowledge some support on numerical aspects with B. Woods and R. Bhai KC at WVU, and helpful discussions and a numerical inversion of (3.18) from J. Egedal. The authors thank F. Pecora, D. Perrone, V. Roytershteyn and L. Sorriso-Valvo for helpful comments on the manuscript. Data for the plots in this paper are available at doi:10.5281/zenodo.3951730. H.L. and G.P.Z. acknowledge support from NSF EPSCoR RII-Track-1 Cooperative Agreement OIA-1655280 and an NSF/DOE Partnership in Basic Plasma Science and Engineering via NSF grant PHY-1707247. H.L., M.H.B. and P.A.C. gratefully acknowledge support from NSF Grant PHY-1804428, NASA Grants NNX16AG76G and 80NSSC19M0146 and DOE Grant DE-SC0020294. S.S. and F.V. acknowledge funding from the European Union Horizon2020 research and innovation programme under grant agreement no. 776262 (AIDA, www.aida-space.eu). This research uses resources of the National Energy Research Scientific Computing Center (NERSC), a DOE Office of Science User Facility supported by the Office of Science of the US Department of Energy under Contract no. DE-AC02-05CH11231.

Editor Francesco Califano thanks the referees for their advice in evaluating this article.

Declaration of interests

The authors report no conflict of interest.

REFERENCES

ADHIKARI, L., ZANK, G. P., HUNANA, P., SHIOTA, D., BRUNO, R., HU, Q. & TELLONI, D. 2017 II. Transport of nearly incompressible magnetohydrodynamic turbulence from 1 to 75 au. *Astrophys. J.* **841** (2), 85.

ADHIKARI, L., ZANK, G. P., ZHAO, L.-L. & WEBB, G. M. 2020 Evolution of entropy and mediation of the solar wind by turbulence. *Astrophys. J.* **891** (1), 34.

ARZAMASSKIY, L., KUNZ, M. W., CHANDRAN, B. D. G. & QUATAERT, E. 2019 Hybrid-kinetic simulations of ion heating in Alfvénic turbulence. *Astrophys. J.* **879** (1), 53.

BANDYOPADHYAY, R., CHASAPIS, A., CHHIBER, R., PARASHAR, T. N., MARUCA, B. A., MATTHAEUS, W. H., SCHWARTZ, S. J., ERIKSSON, S., LE CONTEL, O., BREUILLARD, H., *et al.* 2018 Solar wind turbulence studies using MMS fast plasma investigation data. *Astrophys. J.* **866** (2), 81.

BELLAN, P. M. 2008 *Fundamentals of Plasma Physics*. Cambridge University Press.

BOLTZMANN, L. 1877 Über die beziehung dem zweiten haubtsatze der mechanischen wärmetheorie und der wahrscheinlichkeitsrechnung resp. dem sätzen über das wäarmegleichgewicht. *Wiener Berichte* **76**, 373–435, in (Boltzmann 1909) Vol. II, paper 42.

BURCH, J. L., MOORE, T. E., TORBERT, R. B. & GILES, B. L. 2016*a* Magnetospheric multiscale overview and science objectives. *Space Sci. Rev*. **199**, 5.

BURCH, J. L., TORBERT, R. B., PHAN, T. D., CHEN, L.-J., MOORE, T. E., ERGUN, R. E., EASTWOOD, J. P., GERSHMAN, D. J., CASSAK, P. A., ARGALL, M. R., *et al.* 2016*b* Electron-scale measurements of magnetic reconnection in space. *Science* **352**, 6290.

BURGESS, D., MÖBIUS, E. & SCHOLER, M. 2012 Ion acceleration at the earth's bow shock. *Space Sci. Rev*. **173**, 5–47.

CERRI, S. S., GROŠELJ, D. & FRANCI, L. 2019 Kinetic plasma turbulence: recent insights and open questions from 3D3V simulations. *Front. Astron. Space Sci*. **6**, 64.

CERRI, S. S., KUNZ, M. W. & CALIFANO, F. 2018 Dual phase-space cascades in 3D hybrid-Vlasov–Maxwell turbulence. *Astrophys. J*. **856** (1), L13.

DRAKE, J. F., SWISDAK, M., PHAN, T. D., CASSAK, P. A., SHAY, M. A., LEPRI, S. T., LIN, R. P., QUATAERT, E. & ZURBUCHEN, T. H. 2009 Ion heating resulting from pickup in magnetic reconnection exhausts. *J. Geophys. Res*. **114**, A05111.

DRAKE, J. F., SWISDAK, M., SCHOEFFLER, K. M., ROGERS, B. N. & KOBAYASHI, S. 2006 Formation of secondary islands during magnetic reconnection. *Geophys. Res. Lett*. **33**, L13105.

DU, S., ZANK, G. P., LI, X. & GUO, F. 2020 Energy dissipation and entropy in collisionless plasma. *Phys. Rev.* E **101**, 033208.

EGEDAL, J., LE, A. & DAUGHTON, W. 2013 A review of pressure anisotropy caused by electron trapping in collisionless plasma, and its implications for magnetic reconnection. *Phys. Plasmas* **20**, 061201.

EYINK, G. L. 2018 Cascades and dissipative anomalies in nearly collisionless plasma turbulence. *Phys. Rev.* X **8**, 041020.

FELDMAN, W. C., BAME, S. J., GARY, S. P., GOSLING, J. T., MCCOMAS, D., THOMSEN, M. F., PASCHMANN, G., SCKOPKE, N., HOPPE, M. M. & RUSSELL, C. T. 1982 Electron heating within the earth's bow shock. *Phys. Rev. Lett*. **49**, 199–201.

FUSELIER, S. A., PETRINEC, S. M., SAWYER, R. P., MUKHERJEE, J. & MASTERS, A. 2020 Suppression of magnetic reconnection at Saturn's low-latitude magnetopause. *J. Geophys. Res. Space Phys*. **125** (5), e2020JA027895.

GARY, S. P., ZHAO, Y., HUGHES, R. S., WANG, J. & PARASHAR, T. N. 2018 Species entropies in the kinetic range of collisionless plasma turbulence: particle-in-cell simulations. *Astrophys. J*. **859** (2), 110.

GINGELL, I., SCHWARTZ, S. J., BURGESS, D., JOHLANDER, A., RUSSELL, C. T., BURCH, J. L., ERGUN, R. E., FUSELIER, S., GERSHMAN, D. J., GILES, B. L., *et al.* 2017 MMS observations and hybrid simulations of surface ripples at a marginally quasi-parallel shock. *J. Geophys. Res. Space Phys*. **122** (11), 11003–11017.

GOLDMAN, M. V., NEWMAN, D. L., EASTWOOD, J. P. & LAPENTA, G. 2020 Multi-beam energy moments of multibeam particle velocity distributions. arXiv:2005.09113.

GOODRICH, K. A., ERGUN, R., SCHWARTZ, S. J., WILSON, L. B. III, NEWMAN, D., WILDER, F. D., HOLMES, J., JOHLANDER, A., BURCH, J., TORBERT, R., *et al.* 2018 MMS observations of electrostatic waves in an oblique shock crossing. *J. Geophys. Res. Space Phys*. **123** (11), 9430–9442.

GOSLING, J. T. 2007 *Encyclopedia of the Solar Wind*, chap. 12. Elsevier.

GRECO, A., VALENTINI, F., SERVIDIO, S. & MATTHAEUS, W. H. 2012 Inhomogeneous kinetic effects related to intermittent magnetic discontinuities. *Phys. Rev.* E **86** (6), 066405.

GROŠELJ, D., CERRI, S. S., NAVARRO, A. B., WILLMOTT, C., TOLD, D., LOUREIRO, N. F., CALIFANO, F. & JENKO, F. 2017 Fully kinetic versus reduced-kinetic modeling of collisionless plasma turbulence. *Astrophys. J*. **847** (1), 28.

GUO, X., SIRONI, L. & NARAYAN, R. 2017 Electron heating in low-mach-number perpendicular shocks. I. Heating mechanism. *Astrophys. J*. **851** (2), 134.

HESSE, M., CHEN, L. J., LIU, Y.-H., BESSHO, N. & BURCH, J. L. 2017 Population mixing in asymmetric magnetic reconnection with a guide field. *Phys. Rev. Lett*. **118**, 145101.

HEYVAERTS, J. & PRIEST, E. R. 1983 Coronal heating by phase-mixed shear Alfvén waves. *Astron. Astrophys*. **117**, 220–234.

HOWES, G. G., COWLEY, S. C., DORLAND, W., HAMMETT, G. W., QUATAERT, E. & SCHEKOCHIHIN, A. A. 2006 Astrophysical gyrokinetics: basic equations and linear theory. *Astrophys. J*. **651** (1), 590.

HSU, J.-Y., JOYCE, G. & MONTGOMERY, D. 1974 Thermal relaxation of a two-dimensional plasma in a d.c. magnetic field. Part 2. Numerical simulation. *J. Plasma Phys*. **12** (1), 27–31.

KAUFMANN, R. L. & PATERSON, W. R. 2009 Boltzmann *h* function and entropy in the plasma sheet. *J. Geophys. Res*. **114**, A00D04.

KAUFMANN, R. L. & PATERSON, W. R. 2011 Entropy distribution in the plasma sheet. *J. Geophys. Res*. **116**, A08206.

KAWAZURA, Y., BARNES, M. & SCHEKOCHIHIN, A. A. 2019 Thermal disequilibration of ions and electrons bycollisionless plasma turbulence. *PNAS* **116**, 771.

KLIMCHUK, J. A. 2006 On solving the coronal heating problem. *Solar Phys*. **234**, 41–77.

KROMMES, J. A. & HU, G. 1994 The role of dissipation in the theory and simulations of homogeneous plasma turbulence, and resolution of the entropy paradox. *Phys. Plasmas* **1** (10), 3211–3238.

LE, A., EGEDAL, J., DAUGHTON, W., FOX, W. & KATZ, N. 2009 Equations of state for collisionless guide-field reconnection. *Phys. Rev. Lett*. **102**, 085001.

LEUBNER, M. P. 2004 Fundamental issues on kappa-distributions in space plasmas and interplanetary proton distributions. *Phys. Plasmas* **11**, 1308.

LEVY, R. H., PETSCHEK, H. E. & SISCOE, G. L. 1964 Aerodynamic aspects of magnetospheric flow. *AIAA J*. **2**, 2065.

LIANG, H., CASSAK, P. A., SERVIDIO, S., SHAY, M. A., DRAKE, J. F., SWISDAK, M., ARGALL, M. R., DORELLI, J. C., SCIME, E. E., MATTHAEUS, W. H., *et al.* 2019 Decomposition of plasma kinetic entropy into position and velocity space and the use of kinetic entropy in particle-in-cell simulations. *Phys. Plasmas* **26** (8), 082903.

LIANG, H., CASSAK, P. A., SWISDAK, M. & SERVIDIO, S. accepted Estimating effective collision frequency and kinetic entropy uncertainty in particle-in-cell simulations. *J. Phys.: Conf. Ser*.

LOUREIRO, N. F., SCHEKOCHIHIN, A. A. & ZOCCO, A. 2013 Fast collisionless reconnection and electron heating in strongly magnetized plasmas. *Phys. Rev. Lett*. **111**, 025002.

MATTHAEUS, W. H., YANG, Y., WAN, M., PARASHAR, T. N., BANDYOPADHYAY, R., CHASAPIS, A., PEZZI, O. & VALENTINI, F. 2020 Pathways to dissipation in weakly collisional plasmas. *Astrophys. J*. **891**, 101.

MATTHAEUS, W. H., ZANK, G. P., OUGHTON, S., MULLAN, D. J. & DMITRUK, P. 1999*a* Coronal heating by magnetohydrodynamic turbulence driven by reflected low-frequency waves. *Astrophys. J. Lett*. **523** (1), L93.

MATTHAEUS, W. H., ZANK, G. P., SMITH, C. W. & OUGHTON, S. 1999*b* Turbulence, spatial transport, and heating of the solar wind. *Phys. Rev. Lett*. **82** (17), 3444.

MCANDREWS, H. J., OWEN, C. J., THOMSEN, M. F., LAVRAUD, B., COATES, A. J., DOUGHERTY, M. K. & YOUNG, D. T. 2008 Evidence for reconnection at Saturn's magnetopause. *J. Geophys. Res. Space Phys*. **113** (A4), A04210.

MONTGOMERY, D. & NIELSON, C. W. 1970 Thermal relaxation in one- and two- dimensional plasma models. *Phys. Fluids* **13**, 1405.

MOUHOT, C. & VILLANI, C. 2011 On landau damping. *Acta Math*. **207** (1), 29–201.

NAKARIAKOV, V. M., OFMAN, L., DELUCA, E. E., ROBERTS, B. & DAVILA, J. M. 1999 Trace observation of damped coronal loop oscillations: implications for coronal heating. *Science* **285** (5429), 862–864.

NAKATA, M., WATANABE, T.-H. & SUGAMA, H. 2012 Nonlinear entropy transfer via zonal flows in gyrokinetic plasma turbulence. *Phys. Plasmas* **19** (2), 022303.

NARIYUKI, Y. 2011 On entropy-maximized velocity distributions in circularly polarized finite amplitude Alfvén waves. *Phys. Plasmas* **18** (5), 052112.

NG, J., EGEDAL, J., LE, A., DAUGHTON, W. & CHEN, L.-J. 2011 Kinetic structure of the electron diffusion region in antiparallel magnetic reconnection. *Phys. Rev. Lett*. **106**, 065002.

NUMATA, R. & LOUREIRO, N. F. 2015 Ion and electron heating during magnetic reconnection in weakly collisional plasmas. *J. Plasma Phys*. **81**, 305810201.

OLIVIER, C. P., ENGELBRECHT, N. E. & STRAUSS, R. D. 2019 Permutation entropy analysis of magnetic field turbulence at 1au revisited. *J. Geophys. Res. Space Phys*. **124** (1), 4–18.

OSMANE, A., DIMMOCK, A. P. & PULKKINEN, T. I. 2019 Jensen-Shannon complexity and permutation entropy analysis of geomagnetic auroral currents. *J. Geophys. Res. Space Phys*. **124** (4), 2541–2551.

PARASHAR, T. N. & GARY, S. P. 2019 Dissipation of kinetic Alfvénic turbulence as a function of ion and electron temperature ratios. *Astrophys. J*. **882** (1), 29.

PARASHAR, T. N., MATTHAEUS, W. H. & SHAY, M. A. 2018 Dependence of kinetic plasma turbulence on plasma β. *Astrophys. J*. **864** (1), L21.

PARKS, G. K., LEE, E., MCCARTHY, M., GOLDSTEIN, M., FU, S. Y., CAO, J. B., CANU, P., LIN, N., WILBER, M., DANDOURAS, I., *et al.* 2012 Entropy generation across earth's collisionless bow shock. *Phys. Rev. Lett*. **106**, 061102.

PEZZI, O. 2017 Solar wind collisional heating. *J. Plasma Phys*. **83** (3), 555830301.

PEZZI, O., PERRONE, D., SERVIDIO, S., VALENTINI, F., SORRISO-VALVO, L. & VELTRI, P. 2019 Proton-proton collisions in the turbulent solar wind: hybrid Boltzmann-Maxwell simulations. *Astrophys. J*. **887** (2), 208.

PEZZI, O., VALENTINI, F. & VELTRI, P. 2016 Collisional relaxation of fine velocity structures in plasmas. *Phys. Rev. Lett*. **116**, 145001.

PEZZI, O., LIANG, H., JUNO, J., CASSAK, P. A., SERVIDIO, S., VÁSCONEZ, C. L., SORRISO-VALVO, L., PERRONE, D., ROYTERSHTEYN, V., TENBARGE, J., *et al.* in preparation Dissipation measures in weakly-collisional plasmas. *J. Plasma Phys*.

ROWAN, M. E., SIRONI, L. & NARAYAN, R. 2019 Electron and proton heating in transrelativistic guide field reconnection. *Astrophys. J*. **873** (1), 2.

SARAZIN, Y., DIF-PRADALIER, G., ZARZOSO, D., GARBET, X., GHENDRIH, P. & GRANDGIRARD, V. 2009 Entropy production and collisionless fluid closure. *Plasma Phys. Control. Fusion* **51**, 115003.

SCHEKOCHIHIN, A. A., COWLEY, S. C., DORLAND, W., HAMMETT, G. W., HOWES, G. G., QUATAERT, E. & TATSUNO, T. 2009 Astrophysical gyrokinetics: kinetic and fluid turbulent cascades in magnetized weakly collisional plasmas. *Astrophys. J. Suppl*. **182** (1), 310.

SERVIDIO, S., CHASAPIS, A., MATTHAEUS, W. H., PERRONE, D., VALENTINI, F., PARASHAR, T. N., VELTRI, P., GERSHMAN, D., RUSSELL, C. T., GILES, B., *et al.* 2017 Magnetospheric multiscale observation of plasma velocity-space cascade: hermite representation and theory. *Phys. Rev. Lett*. **119** (20), 205101.

SLAVIN, J. A., ACUÑA, M. H., ANDERSON, B. J., BAKER, D. N., BENNA, M., BOARDSEN, S. A., GLOECKLER, G., GOLD, R. E., HO, G. C., KORTH, H., *et al.* 2009 Messenger observations of magnetic reconnection in Mercury's magnetosphere. *Science* **324** (5927), 606–610.

SONNERUP, B. U. Ö. 1979 Magnetic field reconnection. In *Solar System Plasma Physics* (ed. L. J. Lanzerotti, C. F. Kennel & E. N. Parker), vol. 3, p. 46. North Halland Publishing Co.

TATSUNO, T., DORLAND, W., SCHEKOCHIHIN, A. A., PLUNK, G. G., BARNES, M., COWLEY, S. C. & HOWES, G. G. 2009 Nonlinear phase mixing and phase-space cascade of entropy in gyrokinetic plasma turbulence. *Phys. Rev. Lett*. **103** (1), 015003.

TENBARGE, J. M. & HOWES, G. G. 2013 Current sheets and collisionless damping in kinetic plasma turbulence. *Astrophys. J. Lett*. **771**, L27.

TORBERT, R. B., BURCH, J. L., PHAN, T. D., HESSE, M., ARGALL, M. R., SHUSTER, J., ERGUN, R. E., ALM, L., NAKAMURA, R., GENESTRETI, K. J., *et al.* 2018 Electron-scale dynamics of the diffusion region during symmetric magnetic reconnection in space. *Science* **362** (6421), 1391–1395.

VAIVADS, A., RETINÓ, A., SOUCEK, J., KHOTYAINTSEV, Y. V., VALENTINI, F., ESCOUBET, C. P., ALEXANDROVA, O., ANDRÉ, M., BALE, S. D., BALIKHIN, M., *et al.* 2016 Turbulence heating observer - satellite mission proposal. *J. Plasma Phys*. **82** (5).

VALENTINI, F., PERRONE, D., STABILE, S., PEZZI, O., SERVIDIO, S., DE MARCO, R., MARCUCCI, F., BRUNO, R., LAVRAUD, B., DE KEYSER, J., *et al.* 2016 Differential kinetic dynamics and heating of ions in the turbulent solar wind. *New J. Phys*. **18** (12), 125001.

VASYLIUNAS, V. M. 1983 *Plasma Distribution and Flow* (ed. A. J. Dessler), chap. 395. Cambridge University Press.

WATANABE, T.-H. & SUGAMA, H. 2004 Kinetic simulation of steady states of ion temperature gradient driven turbulence with weak collisionality. *Phys. Plasmas* **11** (4), 1476–1483.

WECK, P. J., SCHAFFNER, D. A., BROWN, M. R. & WICKS, R. T. 2015 Permutation entropy and statistical complexity analysis of turbulence in laboratory plasmas and the solar wind. *Phys. Rev.* E **91**, 023101.

ZANK, G. P., ADHIKARI, L., HUNANA, P., TIWARI, S. K., MOORE, R., SHIOTA, D., BRUNO, R. & TELLONI, D. 2018 Theory and transport of nearly incompressible magnetohydrodynamic turbulence. IV. Solar coronal turbulence. *Astrophys. J.* **854** (1), 32.

ZEILER, A., BISKAMP, D., DRAKE, J. F., ROGERS, B. N., SHAY, M. A. & SCHOLER, M. 2002 Three-dimensional particle simulations of collisionless magnetic reconnection. *J. Geophys. Res.* **107** (A), 1230.

ZHDANKIN, V., UZDENSKY, D. A., WERNER, G. R. & BEGELMAN, M. C. 2019 Electron and ion energization in relativistic plasma turbulence. *Phys. Rev. Lett.* **122**, 055101.